Crystal resorption as a driver for mush maturation: an experimental investigation

Martin F. Mangler[1,*], Madeleine C.S. Humphreys[1], Alexander A. Iveson[1,$], Kari M. Cooper[2], Michael A. Clynne[3], Amanda Lindoo[1,4], Richard A. Brooker[4], Fabian B. Wadsworth[5]

[1]Department of Earth Sciences, Durham University, Durham DH1 3LE, UK

[2]Department of Earth and Planetary Sciences, University of California, Davis, Davis CA 95616, USA

[3]US Geological Survey, Volcano Science Center, Moffett Field, CA 94035, USA

[4]School of Earth Sciences, University of Bristol, Bristol BS8 1RJ, UK

[5]Durham, U.K.

*corresponding author. Current address: School of Earth & Environmental Sciences, University of St Andrews, St. Andrews KY16 9TS, UK

[$]current address: Pacific Northwest National Laboratory, Richland WA 99352, USA

Corresponding author email: martin.mangler@durham.ac.uk

Abstract

The thermal state of a magma reservoir controls its physical and rheological properties: at storage temperatures close to the liquidus, magmas are dominated by melt and therefore mobile, while at lower temperatures, magmas are stored as a rheologically locked crystal network with interstitial melt (crystal mush). Throughout the lifetime of a magmatic system, temperature fluctuations drive transitions between mush-dominated and melt-dominated conditions. For example, magma underplating or recharge into a crystal mush supplies heat,

leading to mush disaggregation and an increase in melt fraction via crystal resorption, before subsequent cooling reinstates a crystal mush via crystal accumulation and recrystallisation. Here, we examine the textural effects of such temperature-driven mush reprocessing cycles on the crystal cargo. We conducted high-P-T resorption experiments during which we nucleated, grew, resorbed, and recrystallised plagioclase crystals in a rhyolitic melt, imposing temperature fluctuations typical for plumbing systems in intermediate arc volcanoes (20-40°C). The experiments reproduce common resorption textures and show that plagioclase dissolution irreversibly reduces 3D crystal aspect ratios, leading to more equant shapes. Comparison of our experimental results with morphologies of resorbed and unresorbed plagioclase crystals from Mount St. Helens (USA) reveals a consistent trend in natural rocks: unresorbed plagioclase crystals (found in Mount St. Helens dacite, basalt and quenched magmatic inclusions) have tabular shapes, while plagioclase crystals with one or more resorption horizons (found in Mount St. Helens dacite, quenched magmatic inclusions, and mush inclusions) show more equant shapes. Plagioclase crystals showing pervasive resorption (found in the dacite and mush inclusions) have even lower aspect ratios. We therefore suggest that crystal mush maturation results in progressively more equant crystal shapes: the shapes of plagioclase crystals in a magma reservoir will become less tabular every time they are remobilised and resorbed. This has implications for magma rheology and, ultimately, eruptibility, as crystal shape controls the maximum packing fraction and permeability of a crystal mush. We hypothesise that a mature mush with more equant crystals due to multiple resorption-recrystallisation events will be more readily remobilised than an immature mush comprising unresorbed, tabular crystals. This implies that volcanic behaviour and pre-eruptive magmatic timescales may vary systematically during thermal maturation of a crustal magmatic system, with large eruptions due to rapid wholesale remobilisation of mushy reservoirs being more likely in thermally mature systems.

Introduction

Crystal textures in igneous rocks offer a rich record of their magmatic history. The stability and composition of a mineral phase in a melt depends on magma conditions (i.e., melt composition, volatile content, oxygen fugacity, pressure and temperature); hence, crystals dissolve, grow, and diffusively equilibrate in response to changing magmatic environments. Compositional zonation and resorption horizons in phenocrysts can therefore help reconstruct up to hundreds of thousands of years of magmatic reservoir dynamics (e.g., Grove et al., 1984; Chakraborty, 2008; Cooper and Reid, 2003; Dohmen et al., 2017; Cooper, 2019; Costa et al., 2020; Petrone and Mangler, 2021) provided that crystal textures can be robustly correlated with specific processes (Vance, 1965; Anderson, 1984; Pearce and Kolisnik, 1990; Ginibre et al., 2007; Rutherford and Devine, 2008; Streck, 2008; Bennett et al., 2019). However, crystals are not merely passive recorders of magmatic histories: crystal numbers, sizes, and shapes themselves affect magma rheology and mobility (Lejeune and Richet, 1995; Caricchi et al., 2007; Mueller et al., 2010; Mueller et al., 2011; Mader et al., 2013; Moitra and Gonnermann, 2015; Arzilli et al., 2022). Crystal shape is a crucial, yet poorly constrained, parameter affecting the rheological properties of a magma. The crystallinity at which a magma becomes rheologically "locked" is commonly described as the maximum packing fraction φ_m (e.g., Mueller et al., 2010; Mader et al., 2013) and is often assumed to be 0.4-0.5 in models and conceptual works (e.g., Bachmann and Bergantz, 2006; Huber et al., 2011; Gelman et al., 2013; Cooper and Kent, 2014). However, φ_m strongly depends on crystal shape and can vary from 0.1 for very high or low aspect ratios to 0.74 for spheres (Mueller et al., 2010, 2011; Mader et al., 2013). Crystal morphology is therefore a key variable controlling whether an interlocking crystal mush will form in a crystallising magma reservoir, and, in crystal-rich systems, how easily (and rapidly) the crystal mush can be unlocked. Hence, to better understand magma reservoir dynamics, it is important to determine crystal

shapes in magma reservoirs and their sensitivity to common magmatic processes. Here, in light of the abundance of resorption horizons and overgrowth in most igneous crystals, we experimentally examined the effects of resorption and recrystallisation on plagioclase crystal shapes. Experiments were designed to study plagioclase growth and resorption under magmatic conditions approximating storage beneath intermediate arc volcanoes such as Mount St. Helens, Washington, USA (MSH). Experimental crystal morphologies were then compared to a new database of plagioclase shapes in MSH rocks, including a dacite from the 1982 lava dome, a Castle Creek age basalt, and a range of mush inclusions and quenched magmatic inclusions (QMI). Our work suggests that resorption reduces crystal aspect ratios, and this maturation of the crystal cargo facilitates mush remobilisation and formation of an eruptible magma.

Terminology

Resorption: Congruent dissolution of a crystal. Unless otherwise specified, the terms *resorption* and *dissolution* are used interchangeably in this work. *Surficial resorption* is the focus of this study and refers to dissolution of the exterior of euhedral crystals producing rounded or embayed crystals; minor dissolution surfaces within crystals reflect surficial resorption events earlier in the crystal growth history (Fig. 1a). *Pervasive resorption* refers to extensive dissolution affecting crystal interiors and obscuring original crystal shapes (Fig. 1b). This includes sieved, dusty, boxy-cellular, and spongy-cellular textures (Streck, 2008), but also deep embayments and dissolution along twinning planes.

Crystal shape: The 3D shape of a crystal, expressed as the 3D short/intermediate growth dimension ratio (*S/I*). This 3D shape factor can be accurately determined using 2D intersection widths and lengths and the 2D-to-3D projection software *ShapeCalc* (Mangler et al., 2022). Crystals with *low S/I* (i.e., $S<<I$) are *tabular* (i.e., book-shaped) and typically show *high aspect ratios* in 2D (Fig. 1c). Crystals with *high S/I* (i.e., $S\approx I$) are typically *equant* in 2D cross-sections and are here referred to as having *low aspect ratios* (Fig. 1d). The terms *shape* and *morphology* are used interchangeably in this work.

Crystal texture: Morphological characteristics (e.g., shape, size, and zoning) of a crystal or crystal population. Note that textural and compositional characteristics are often correlated (i.e., zoning).

Mush maturity: As a concept alternative to ages, *mush maturity* describes the number of individual events that have disturbed the system and resulted in resorption and recrystallisation. Such events may be driven by punctuated heating events, convective self-mixing (Couch et al., 2001), influx of fresh magma or volatiles, or extraction of material during eruptions, and they are collectively termed *remobilisation* events in this work. Note that resorption and recrystallisation can also occur in situ, i.e., without the mush being remobilised, for example via reactive porous flow (e.g., Boulanger and France, 2023).

Surface roughness: The topographic relief of the crystal surface at length scales ≥1µm; i.e., the amplitude deviation from a corresponding smooth crystal facet. *Surface roughness* is expressed as the ratio of 2D crystal perimeter and 2D crystal area normalised to an unresorbed crystal.

Interface roughness: The structure of the crystal surface on an atomic level (Kossel, 1927; Stranski, 1928; Hartman and Perdok, 1955; Jackson, 1958; Kirkpatrick, 1975; see Sunagawa, 2007 for a summary). A smooth interface has an atomically flat surface with few steps; a rough interface is characterised by a high density of kinks and steps. Interface roughness varies across different faces of a crystal. Since steps and kinks have lower attachment energies than flat surfaces, the degree of interface roughness controls crystal growth mechanisms and rates.

Magma storage beneath Mount St. Helens

Mount St. Helens volcano was chosen as a case study to compare with our experiments because it is one of the most studied examples of arc volcanism, and its plumbing system architecture and dynamics are relatively well understood (e.g., Sherrod et al., 2008). In brief, crystal compositions and textures have been used to reconstruct a deep, mafic to intermediate mush zone hosting geochemically diverse magma batches (Blatter et al., 2017; Humphreys et al., 2019; Wanke et al., 2019a, b; Keller et al., 2024), and a heterogeneous mid- to upper-crustal mush zone which is frequently disrupted, partially digested and hybridised by magma recharge (Gardner et al., 1995a, b; Pallister et al., 2008; Rutherford and Devine, 2008;

Claiborne et al., 2010; Cashman and Blundy, 2013). Thermal storage histories of plagioclase crystals at Mount St. Helens, derived from U-series disequilibria and diffusion chronometry (Cooper and Reid, 2003; Cooper and Donnely, 2008; Schlieder et al., 2022), indicate that a significant proportion of crystals was stored for >10 kyrs at relatively low temperatures of ≤750°C (i.e., in a crystal mush, Cooper and Kent, 2014), punctuated by short periods at elevated temperatures (i.e., in a melt-dominated, eruptible state). This view is consistent with textural studies (Berlo et al., 2007; Streck et al., 2008; Cashman and Blundy, 2013), which suggest that temperature fluctuations are the primary cause for abundant surficial and pervasive resorption textures, such as dissolution surfaces within crystals (Fig. 1a) and cellular crystal cores (Fig. 1b). Temperature fluctuations have been described by Cashman and Blundy (2013) as the "inevitable consequence of incremental, or pulsed, assembly of crustal magma bodies wherein each pulse interacts with ancestral, stored magmas." Based on their petrological models, Cashman and Blundy (2013) inferred the magnitude of the temperature fluctuations in the magma reservoir beneath MSH to be on the order of 20-40°C. Importantly, textural evidence for mixing between mafic and evolved magmas at MSH is relatively rare, and it has been described as a chemically closed system (Cashman and Blundy, 2013). Temperature fluctuations are therefore likely to be a key driver of crystal maturation during storage at MSH.

Previous experimental work on crystal textures in magma reservoirs

Phase equilibrium experiments have constrained the effects of melt composition, temperature, pressure, and H_2O content on mineral composition and stability (e.g., Geschwind and Rutherford, 1992; Sisson and Grove, 1993; Gardner et al., 1995a; Panjasawatwong et al., 1995; Danyushevsky, 2001; Kohut and Nielsen, 2003; Blatter et al., 2017; Waters and Lange, 2017), and progress has been made in understanding late-stage mineral breakdown and

crystallisation during ascent and emplacement through decompression and cooling experiments (e.g., Lofgren, 1974; Nelson and Montana, 1992; Rutherford and Hill, 1993; Hammer and Rutherford, 2002; Martel and Schmidt, 2003; Kohut and Nielsen, 2004; Shea and Hammer, 2013; Riker et al., 2015; Waters et al., 2015; Giuliani et al., 2020). However, experiments studying crystal textures that form in response to temperature, pressure and compositional variations representative for magma reservoir dynamics are relatively rare.

A particular focus of previous experiments was to reproduce sieve textures in plagioclase, which was achieved by melting of plagioclase crystals in air (Tsuchiyama and Takahashi, 1983) by immersing crystals in basaltic melts (Lofgren and Norris, 1981) or synthetic Di-Ab-An glasses (Tsuchiyama, 1985; Nakamura and Shimakita, 1998), and by basalt-gneiss assimilation experiments (Castro, 2001). All studies produced similar sieve textures; however, contrasting formation mechanisms were proposed. Tsuchiyama (1985) suggested incongruent melting of plagioclase, whereas Nakamura and Shimakita (1998) rejected this hypothesis, as it would require unrealistically high diffusion rates in plagioclase, and instead suggested congruent melting and recrystallisation. The textures produced in these experiments resemble typical boxy-cellular textures observed in natural rocks including MSH, which led Cashman and Blundy (2013) to follow Tsuchiyama (1985) to explain the boxy-cellular cores at MSH. However, the origin of boxy-cellular textures remains disputed, with other workers suggesting they are the result of rapid, skeletal growth of anorthite (An)-rich plagioclase and subsequent infill of the voids with lower-An plagioclase (Berlo et al., 2007; Streck, 2008). In any case, experiments to date do not faithfully reproduce proposed magmatic conditions and processes at MSH, as they did not only vary temperatures but also used variable, predominantly mafic host melt compositions. This may explain why the experiments routinely produced pervasive resorption textures, but less so the more subtle

surficial resorption features typical of many MSH plagioclase crystals (Fig. 1a), which are the primary focus of this study.

Another subject of interest in many petrological studies is the origin of oscillatory zoning (e.g., Pearce and Kolisnik, 1990; L'Heureux and Fowler, 1996; Ginibre et al., 2002). At least two types of oscillatory zoning were previously identified, one of which features resorption surfaces related to oscillations, indicating magma reservoir dynamics as a driving factor (Ginibre et al., 2002). However, oscillatory zoning in plagioclase has only been produced in one slow cooling experiment by Lofgren (1980) and has not been achieved since. Allègre et al. (1981) suggested that relatively large undercoolings and short run durations preclude development of oscillatory zoning under experimental conditions.

To date, no experiments have focused on reproducing the abundant dissolution surfaces found in many igneous crystals under natural magmatic conditions. While temperature cycling experiments have been conducted using alkali basalt (Mills and Glazner, 2013), high-Mg basalt (Marxer et al., 2022), and dacite (Erdmann and Koepke, 2016), these studies focused on melt pool enlargement and crystal coarsening effects, and they did not discuss crystal shapes or internal textures. Here, we ran unseeded, isobaric, closed-system heating and temperature cycling experiments using a hydrated rhyolitic melt to study whether temperature fluctuations typical for the MSH magmatic system can reproduce common surficial resorption textures in plagioclase.

Experimental design

Experiments were designed to reproduce typical magmatic plumbing system processes, i.e., plagioclase crystals grown in a water-saturated silicic melt are exposed to a short-lived temperature increase of 20-40°C. Experiments were conducted at 150 MPa in rapid-quench cold-seal pressure vessels (CSPV) at the University of Durham (UK) using a hydrated Fe-free

rhyolitic starting glass (72.3 wt. % SiO_2, 16.0 % Al_2O_3, 5.25 % Na_2O, 2.91 % K_2O, 1.99 % CaO, 0.67 % MgO, 0.61 % TiO_2, 0.1 % P_2O_5) to approximate interstitial melt compositions at dacitic arc volcanoes. An iron-free composition was chosen as it is insensitive to fO_2 and to ensure that plagioclase is the dominant near-liquidus mineral phase, which allowed us to study the effects of resorption on plagioclase morphology without interference by other phases. Hence, the experiments do not strictly reproduce the MSH mineral assemblage; they do, however, facilitate the study of plagioclase dissolution and growth kinetics at conditions approximating magma storage at intermediate arc volcanoes.

The starting glass was synthesised using reagent-grade oxides and carbonates, and hydrated under experimental starting conditions to ensure water saturation (~5 wt.% H_2O), following Mangler et al. (2023). The liquidus of the water-saturated starting glass is 890 ± 10°C at the experimental pressure of 150 MPa (Mangler et al., 2023), with plagioclase being the liquidus phase. About 30 mg of hydrated starting glass chips were loaded into $Au_{80}Pd_{20}$ capsules of ~15 mm length and 2.6 mm inner diameter; an additional 3 µL MilliQ® ultrapure water was added to the capsule to maintain water saturation during heating experiments. The use of glass chips instead of powder limits nucleation and favours fewer, larger crystals (Mangler et al., 2023). The capsules were weighed, welded shut using a Lampert PUK 5.1 arc welder, heated at 110°C for 30 min and weighed again to check for leaks. Capsule masses were also recorded post-experiment, with any that showed mass changes of >±1 mg assumed to have leaked and therefore discarded. For each experiment, one capsule was loaded into high-performance INCONEL 713LC autoclaves. The CSPV assembly was pressurised using water as pressurising medium and the furnace heated to experimental temperatures before inserting the capsule into the hot zone of the furnace, establishing experimental starting conditions of 870°C and 150 MPa in the sample within seconds. Temperature was monitored using an N type thermocouple (located <5 mm from the centre of the capsule; ±2.2°C accuracy) and

controlled remotely via a Eurotherm nanodac controller, and pressure was monitored with a WIKA digital pressure transducer (reproducibility <1 bar).

Each experiment was held at 870°C (i.e., an undercooling ΔT of 20°C) and 150 MPa for one week (168 hours) to grow plagioclase crystals (Fig. 2). Afterwards, temperature was increased to 890°C (ΔT = 0°C; 23-CSB-04), 900°C (i.e., a superheating of ΔT = -10°C; 23-CSB-03), and 910°C (ΔT = -20°C 23-CSB-07), respectively. The temperature increase of 20-40°C was achieved within 15 minutes, during which pressure was manually adjusted to remain stable at 150 MPa. Each experiment was held at respective elevated temperatures for another 168 hours before quenching, which was achieved by pulling the capsule into a water-cooled sleeve (12°C). In one experiment (23-CSB-05), an additional step was introduced to complete a 30°C temperature cycle: the temperature was returned to its initial conditions of 870°C for another week after being held at 900°C for 168 hours (Fig. 2). A baseline experiment (22-CSB-03) was quenched after the first 168 hours at 870°C to establish the textural characteristics of the initial plagioclase population; this experiment has previously been described in Mangler et al. (2023).

Analytical methods

Scanning electron microscopy

Experimental run products were surveyed using a polarising microscope before mounting in EpoFix epoxy resin for scanning electron microscope (SEM) analysis. Back-scattered electron (BSE) maps of each experimental charge were acquired at Durham University on a Hitachi SU-70 field emission scanning electron microscope, using 15 kV accelerating voltage, 15 mm working distance, 40-60 µs dwell time, and 300-2500x magnification, depending on crystal size and number density. Single BSE images were montaged into larger maps using Oxford Instruments' AZtec® software. In addition to experimental run products, BSE images were acquired of eight MSH samples (a 1982 dome dacite, a Castle Creek age

basalt, three dacite-hosted quenched mafic inclusions and three dacite-hosted mush inclusions) for comparison of plagioclase textures.

Plagioclase, melt inclusion, boundary layer, and host glass compositions (Si, Al, Fe, Mg, Ca, Na, K, Sr) were measured by energy-dispersive X-ray spectroscopy (EDS) using an Oxford Instruments X-Max^N 50 mm^2 Silicon Drift Detector mounted on the Hitachi SU-70. Quantitative EDS analysis is achieved using a standardisation database pre-installed in AZtec® (Pinard et al., 2020) with an energy calibration performed on a pure element Mn standard, and a beam calibration performed on a pure element Cu standard. Spot analyses were acquired with a livetime of 10s, process time of 3, and energy range of 20 keV; line measurements were acquired using the same conditions and a livetime of 70s. The spatial resolution of EDS analyses is ~1 µm^2, which is smaller than the size of the textural features studied in this work. Standard errors of EDS analyses are <5% for major elements; analysis of secondary plagioclase standards (Smithsonian labradorite NMNH 115900 and anorthite NMNH 137041) yielded a reproducibility of ±1.5 mol% An and mean An values within 3.5 mol% of the accepted values and (2 SD; Supplementary Material S1.2).

Textural analysis

All crystals fully enclosed on BSE maps (n_{plag} = 125-613) were manually outlined using image processing software ImageJ (Schneider et al. 2012). Crystal intersection areas and perimeters as well as 2D intersection lengths (l) and widths (w) were extracted using ImageJ's best fit ellipse algorithm. For Mount St. Helens samples, plagioclase crystals that were clearly xenocrystic or severely intergrown were omitted, and in 1982 dacite sample MSH90-9, crystals >100 µm length were targeted because smaller crystals are related to ascent-driven crystallisation (Mangler et al., 2022), which is not the focus of this study. For MSH 1982 dacite samples MSH90-9, aspect ratios of crystal cores and mantles were

283 determined using line measurements in ImageJ, which yields results directly comparable to
284 data derived from outline measurements (Mangler et al., 2022).
285 Average crystal volume in a sample is calculated following Mangler et al. (2023) as

286 $$V_{plag,av} = \sqrt{\frac{{A_{plag}}^3}{{n_{plag}}^3}}$$

287 where A_{plag} is the total area of n_{plag} crystals measured in the sample. Crystal shapes were
288 estimated from 2D *l* and *w* data using 2D-to-3D projection software ShapeCalc (Mangler et
289 al., 2022). Crystal morphologies are expressed as the ratio of 3D short/intermediate crystal
290 dimensions (*S*/*I*), since 3D crystal length (*L*) is poorly constrained by 2D intersection data
291 (Higgins, 2000). Surface roughness is expressed as the ratio of 2D crystal perimeter and 2D
292 crystal area and is reported normalised to the mean value for the unresorbed crystals of static
293 experiment 22-CSB-03. Plagioclase textural data are reported in Supplementary Material
294 S1.1 for experiments, and in Supplementary Material S2.1 for MSH samples.

295 ### *Electron microprobe analysis (EPMA)*

296 Major element (Si, Al, Ca, Na, K) and selected minor element (Ti, Fe, Mg) concentrations in
297 MSH plagioclase crystals were analysed using a Cameca SX100 electron microprobe at the
298 University of Edinburgh. Analyses were run at an acceleration voltage of 15 kV, a beam
299 current of 10 nA (except for Ti, which was analysed in a second stage using a beam current
300 of 100 nA), and a 5 µm beam. Peak counting times were 20 s for all elements except Fe (40
301 s), and background counting times were 50% of peak counting times. Sodium migration was
302 not observed during the first 20 seconds of beam exposure at the chosen conditions, hence Na
303 was measured at the beginning of each analysis. Raw data were calibrated using internal
304 mineral standards including Jadeite (Na, Si), Spinel (Mg, Al), Wollastonite (Ca), Orthoclase
305 (K), Fayalite (Fe), and Rutile (Ti). Repeat measurements of an internal labradorite standard
306 conducted throughout the session yielded a relative variability of ≤3 % (2SD) for major

elements and 8-17 % for minor elements (Supplementary Material S2.2). These values are similar to the relative instrumental standard errors. The accuracy of major element analyses is characterised by relative deviations of <3% from recommended values for USGS reference basaltic glass BCR-2g (Supplementary Material S2.2).

Laser ablation ICP-MS analysis (LA-ICP-MS)

Trace element concentrations in MSH plagioclase crystals were determined by laser ablation ICP-MS using a ThermoFisher Element 2 and an iCAP QQQ ICP-MS coupled with a Teledyne Analyte Excite+ 193 nm laser ablation system. Analyses were made in situ on the same polished thin sections used for EPMA analyses. Each crystal analysed by LA-ICP-MS was also analysed using EPMA, such that major and trace element concentrations could be coupled and LA-ICP-MS data normalised using accurate ^{43}Ca (or ^{29}Si) values. Ablation was conducted using square spot sizes of 30 x 30 µm (MSH-22-56), 40 x 40 µm (MSH90-9) and 50 x 50 µm (all other samples), with an 8 Hz laser repetition rate and 4 mJ pulse energy. Samples were ablated in a helium atmosphere comprising 0.5 L min^{-1} to the main sample chamber and 0.3 L min^{-1} to the sample cup, giving a total sample carrier gas volume of 0.8 L min-1. This was mixed with approximately 1 L min^{-1} Ar as the sample entered the ICP torch. The Ar gas flow rate and torch sampling depth were adjusted to achieve high instrumental sensitivity while maintaining a U/Th ratio close to 1. Samples were ablated for 30 s with backgrounds measured for 30 s before and after each analysis. Analytes and dwell times were ^{7}Li (0.01s), ^{24}Mg (0.01s), ^{31}P (0.01s), ^{43}Ca (0.005s), ^{44}Ca (0.005s), ^{48}Ti (0.05s), ^{55}Mn, ^{57}Fe (0.01s), ^{63}Cu (0.01s), ^{66}Zn (0.01s), ^{85}Rb (0.01s), ^{88}Sr (0.01s), ^{137}Ba (0.01s), ^{139}La (0.1s), ^{140}Ce (0.1s),^{141}Pr (0.1s), ^{146}Nd (0.1s), ^{153}Eu (0.1s), and ^{208}Pb (0.05s). Instrumental standard errors of individual analyses are typically 10-20% (Supplementary Material S2.2). Primary (internal) calibration was performed using USGS reference glasses GSD (for MSH90-9 and MSH-22-56) and BCR-2G (for all other samples). Instrumental drift was monitored using NIST 612

and NIST 610 glass standards. Secondary standards were BCR-2G and StHs-G (MSH90-9) and BHVO-2G (all other samples) and they were run repeatedly throughout the sessions. Relative standard deviations of repeat analyses are generally 6% or less (total range 3.3 – 12 %), and secondary standard analyses generally fall within 6% of accepted values (Supplementary Material S2.2).

Experimental results

Effect of temperature increase on crystal textures and compositions

Plagioclase crystals grown from the hydrous rhyolite melt at 150 MPa and 870°C (ΔT = 20°C) have a mean 2D intersection length of 38 µm and show a tabular morphology, with 2D aspect ratios of ~1:4 under the microscope (Experiment 22-CSB-03; Table 1, Figs. 3a, 4 and 5a; see also the clear mode at w/l = 0.24 in Fig. 4). By contrast, crystals in the heating experiments show dissolution textures which affect their morphologies. Temperature increase to liquidus and super-liquidus conditions results in smaller, more rounded, and less tabular crystals, the effects becoming more pronounced as the heating interval increases (Figs. 2-5; Table 1). Specifically, mean crystal lengths reduce by 35% after one week at the liquidus (890°C; 23-CSB-04), by 44% after one week at 900°C (23-CSB-03), and by 66% after one week at 910°C (23-CSB-07; Table 1, Fig. 5a). At the same time, crystals become less tabular: After a week at 890°C and 900°C, an increased number of crystals show 2D aspect ratios of 1:2.5 to 1:3 (secondary peaks at w/l = 0.35-0.4 in Fig. 4). After a week at 910°C, the majority of crystals show 2D aspect ratios of 1:2.5 (mode at w/l = 0.4), even though many crystals retain the shapes of the original crystal population ($w/l \approx 0.25$; Fig. 4). Frequency distributions are generally flatter for higher temperatures, reflecting an increasing variety of crystal morphologies. Nonetheless, projection of 2D w/l frequency distributions to 3D crystal shapes using *ShapeCalc* (Mangler et al., 2022) also traces the reduction in crystal aspect

ratios, with *S/I* increasing to *S/I* = 0.29 ± 0.03 after one week at 890°C, *S/I* = 0.28 ± 0.04 after one week at 900°C, and *S/I* = 0.36 ± 0.05 after one week at 910°C (Table 1, Fig. 5b).

Back-scattered electron (BSE) images show clear evidence for increasingly diverse crystal morphologies (Figs. 3 & 6). Plagioclase crystals in the static experiment are generally euhedral, although some crystals show melt inclusions along twinning planes (Fig. 3a; cf. Brugger and Hammer, 2015), which suggests melt entrapment during rapid growth. At elevated temperatures, surficial resorption of crystal facets results in more rounded crystals and an increasing macroscopic surface roughness as temperatures increase (Figs. 3 & 5c). Pervasive resorption leads to the disintegration of the original crystals grown at 870°C, predominantly along growth twinning planes (Fig. 3b-d), and some crystals also show embayments extending deep into their interiors (Fig. 6b). By contrast, sieved, dusty, boxy-cellular or spongy-cellular textures are not observed in our experiments. It is striking that not all crystals are affected equally by resorption processes, with some crystals showing minimal dissolution features whereas other crystals in the same experiment are clearly resorbed (Fig. 3).

In terms of mineral compositions, plagioclase shows variability for each experiment, including the static growth experiment 22-CSB-03, and average values overlap (An_{34-42}; Fig. 5; Table 1; Supplementary Material S1.2). However, the experiments that saw an increase in temperature show higher compositional variability and higher average An contents than the static experiment (Fig. 6). High-contrast BSE images reveal that resorbed crystals show domains of varying An contents, with more anorthitic domains often associated with melt inclusions (Fig. 6b & c). Moreover, resorbed crystals show thin rims (typically 1-2 µm) of more anorthitic compositions ($\leq An_{49}$; Figs. 5d & 6; Table 1); the difference between average crystal An concentrations and maximum observed rim An concentrations increases from $\Delta X_{An} = 5$ for a temperature increase of 20°C to $\Delta X_{An} = 12$ for a temperature increase of 40°C

(Fig. 5d). Finally, resorbed plagioclase crystals are surrounded by boundary layer melts, which are typically 2 µm (and up to 3.5 µm) wide and often show elevated Al_2O_3, CaO, and CaO/Na_2O relative to 'far-field' glass at greater distances from crystals (Fig. 7; Table 1).

Effect of temperature cycling on crystal textures and compositions

Temperature increases in magma reservoirs will inevitably be followed by cooling. To reproduce such a temperature cycle, one experiment (23-CSB-05) was cooled back down to initial growth conditions after one week at 900°C and held at 870°C for another week. This temperature cycling experiment resulted in zoned crystals whose lengths and surface roughness approached those of the static experiment 22-CSB-03 (Fig. 8a &c; Table 1). However, 3D crystal shapes in the cycled experiment are less tabular than in the static experiment, with *S/I* aspect ratios identical to the experiment that was quenched directly after the 900°C step (23-CSB-03; Fig. 8b). This indicates that, in contrast to crystal length and surface roughness, crystal shape is not reset to pre-resorption aspect ratios during overgrowth.

Crystal zoning in the cycling experiment is strikingly complex (Figs. 9 & 10; Table 1). Resorbed cores ($An_{37\pm5}$) are surrounded by thin anorthite-rich bands ($An_{44\pm6}$) of varying width (0 - 5 µm), followed by ≤50 µm wide mantles of variable, intermediate An contents ($An_{36\text{-}40}$) containing abundant melt inclusions (Figs. 9a & b). Complex zoning features in plagioclase bands often result in a patchy appearance (Fig. 9a), and some crystals even appear to show two resorption horizons (Fig. 9c), though we interpret this to be the result of 2D sectioning effects. Crystals are commonly intergrown, with zoning patterns indicating that intergrowth occurred at various stages of the experiment: some intergrown crystals show touching cores with melt inclusions at the interface, indicating that they aggregated before or during the temperature increase (Figs. 9c & 10a); other crystals had already started growing mantles before they impinged on each other, suggesting intergrowth during the cooling step of the experiment (Fig. 9a). Moreover, crystals often show more than one core in 2D section.

406 In many cases, separate cores likely reflect crystal disaggregation at elevated temperature
407 (Fig. 10c). In other cases (e.g., Fig. 10b), it is unclear whether these cores are originally
408 separate crystals which were conjoined during cooling-driven overgrowth, or whether they
409 represent 2D intersections of a single crystal with a highly irregular resorbed core. Towards
410 the rims of the zoned plagioclase crystals, compositions approach those of the cores grown at
411 870°C during the first week of the experiment (Fig. 9a), which suggests a return to
412 equilibrium conditions during cooling.

413 # Analysis of resorption experiments

414 ## *Plagioclase dissolution reduces crystal aspect ratios*

415 Our heating experiments clearly trace a progressive change in crystal shape and size during
416 resorption (Fig. 5). This demonstrates that plagioclase dissolution affects different crystal
417 faces differently and, on average, modifies crystal morphologies towards more equant shapes.
418 It is not surprising that dissolution is anisotropic, as both growth and dissolution kinetics
419 depend on the surface energy σ of a crystal facet (e.g., Lasaga, 1998). Since high-energy
420 crystal surfaces are energetically unfavourable, their surface area tends to be minimised
421 during crystal growth as lower-energy surfaces outgrow them. As a result, high-energy
422 surfaces tend to form the smallest facets of a crystal in the direction of fastest crystal growth
423 (i.e., they define the 3D longest dimension). During dissolution, the same high-energy facets
424 will show the highest dissolution rates, as this presents the most effective pathway to reduce
425 the overall surface energy of the crystal. Dissolution kinetics are further accelerated by the
426 relatively higher density of kinks and steps (Hartman and Perdok, 1955) of the high-energy
427 surface, which reduces the activation energy for dissolution (Lasaga and Lüttge, 2004). As a
428 result, the longest crystal dimension dissolves faster than other dimensions, leading to a
429 decrease in 3D aspect ratio. The degree of resorption and shape change increases with the
430 heating interval (Fig. 5), i.e., the extent of disequilibrium imposed on the system. However, it

431 is noteworthy that crystal morphologies do not evolve towards their thermodynamic
432 equilibrium shapes (i.e., the shape that minimises the total free surface energy) during
433 dissolution or growth because kinetics control the process, as suggested by Gibbs (1878) and
434 confirmed by *ab initio* mechanistic models of crystal growth and dissolution rates (Snyder
435 and Doherty, 2007).

436 A key observation in the heating experiments is that dissolution does not affect all crystals
437 equally: some crystals in our experiments are severely affected by resorption, whilst a
438 neighbouring crystal might show relatively little evidence for resorption (e.g., Fig. 3c).
439 Similarly heterogeneous dissolution kinetics and morphologies have been observed and
440 modelled in low-temperature mineral-fluid reaction studies (e.g., Lasaga and Lüttge, 2004;
441 Zhang and Lüttge, 2009; Fischer et al., 2012; Pollet-Villard et al., 2016). Following their
442 work, we suggest that the extent and nature of resorption (at given magmatic conditions) is
443 controlled by nm to µm-scale variations in crystal surface reactivity (cf. Lüttge et al., 2013;
444 Fischer et al., 2014). Surface reactivity correlates with interface roughness: surface domains
445 with a high density of kinks and steps (Hartman and Perdok, 1955), such as discontinuities
446 and defects (i.e., impurities, dislocations, and point defects), have higher reactivities and will
447 therefore dissolve faster than surfaces with a lower density of reactive sites (Blum and
448 Lasaga, 1987; Arvidson et al., 2003; Lasaga and Lüttge, 2004; Fischer et al., 2014; Noiriel et
449 al., 2019; 2020). For example, Lasaga and Lüttge (2001) demonstrated the role of screw
450 dislocations in controlling crystal surface dissolution via the formation of etch pits and steps.
451 This framework of surface defects as a driving force for resorption is consistent with
452 observations of resorbed plagioclase crystals in this study, which show abundant evidence for
453 dissolution focused on features with a higher number of defects, i.e., cracks, growth twinning
454 planes and grain boundaries (Figs. 3, 6, 9, 11a). The observed overall increase in crystal-scale
455 surface roughness with progressing resorption (Fig. 5c) is also consistent with findings from

456 other mineral dissolution studies (Noiriel et al., 2019), who attribute the increase in surface
457 roughness to pit formation. As etch pits grow, they can coalesce (Lasaga and Lüttge, 2001;
458 Arvidson et al., 2003; Lüttge, 2005), which may lead to the formation of macrosteps (Noiriel
459 et al., 2020) and embayments such as those seen in Fig. 6b and Fig. 11b. While these studies
460 consider aqueous systems rather than magmas, we suggest that the variability of crystal
461 shapes in our resorption experiments is consistent with a control by initial crystal shapes and
462 distributions of surface defects. In addition, morphological evolution during resorption has
463 been found to depend on initial crystal size and saturation state (Zhang and Lüttge, 2009),
464 with smaller crystals and, counterintuitively, close-to-equilibrium conditions resulting in
465 more pronounced shape changes. Finally, localized changes in melt chemistry (e.g., due to
466 plagioclase dissolution) result in variable plagioclase saturation states on a small length scale,
467 which ultimately control dissolution and growth kinetics. Such local variations in melt
468 composition are primarily induced by plagioclase dissolution and growth (see below), though
469 some of our experiments also crystallised small amounts of amphibole, biotite,
470 clinopyroxene, and titanite (Supplementary Material S1.1), which could affect local melt
471 chemistry.

472 In summary, despite the variability of individual crystal shapes in our resorption experiments,
473 crystal populations as a whole display a clear trend towards progressively more equant crystal
474 shapes and rougher surfaces during resorption.

475 ### *Plagioclase dissolution and growth from boundary layer melts at elevated*
476 ### *temperatures*

477 Dissolution of plagioclase results in the formation of a boundary layer melt enriched in CaO
478 and Al_2O_3 (Danyushevsky et al., 2001), and the resulting increase in melt Ca/Na surrounding
479 the crystals has been suggested to lead to overgrowth of dissolution surfaces by higher An
480 plagioclase (Streck, 2008). Indeed, boundary layer melt compositions in our experiments, i.e.,

experimental glasses within ~3.5 µm of partly dissolved plagioclase crystals, often show elevated Ca/Na ratios ($CaO/Na_2O \leq 1.2$; Fig. 7; M_1 in Fig. 11b) compared to 'far-field' glass further from the crystal-liquid interface (CaO/Na_2O = 0.3-0.5; Fig. 7; M_0 in Fig. 11; Table 1; Supplementary Material S1.2). The average boundary layer melt composition for the experiment held at 900°C (23-CSB-03) corresponds to a modelled liquidus temperature of ~955°C under water-saturated conditions (Rhyolite-MELTS v.1.2.x; Gualda and Ghiorso, 2015). This suggests moderate undercoolings of ~50°C at the crystal-melt interface, which would favour crystallisation of a higher An plagioclase rim, as observed in our experiments (Fig. 7; Pl_1 in Fig. 11b). The width of the rims in the heating experiments varies between 0 and 2 µm within single crystals, with some domains of the crystal core surfaces completely lacking high-An overgrowth, such that the high-An rim does not generally alter crystal shapes (Figs. 6, 7 & 11b). The localised extent of recrystallisation of the dissolved plagioclase is likely controlled by two factors:

(1) Dissolved plagioclase constituents will be transported away from the crystal-melt interface via elemental diffusion, which will result in a less enriched boundary layer, especially at slow dissolution rates and high temperatures. Similarly, convection of crystals in the melt or melt advection may disrupt the boundary layer and bring crystal surfaces into contact with fresh, lower Ca/Na melt. Both cases would result in reduction or even minimisation of the undercooling at the crystal surface, which would suppress crystallisation. The wide range of boundary layer melt compositions, which covers the entire range of Ca/Na ratios between far-field glass and plagioclase cores (Table 1; Supplementary Material S1.2), suggests that a combination of melt diffusion, crystal transport, and melt advection is effective in the experiments. The surface morphologies of the resorbed crystals likely influence how effectively these processes operate on a µm-scale.

(2) At low to moderate undercoolings, crystal growth is controlled by the availability of nucleation sites (Fletcher, 1958; Chernov, 1984; Liu, 2002). Because kinks and steps (Hartman & Perdok, 1955) on the crystal surface have lower attachment energies than flat surfaces, rough interfaces will grow more readily than smooth interfaces at the undercooling conditions inferred for our boundary layer melts (ΔT ~50°C). The presence or absence of a high-An overgrowth in our experiments may therefore depend, in part, on the local interface roughness.

Plagioclase dissolution kinetics have previously been attributed to NaSi-CaAl diffusion in the crystals and incongruent melting of Ab and An components (Tsuchiyama, 1985). However, numerous studies have since concluded that plagioclase dissolution occurs via congruent dissolution and recrystallisation (Wark and Watson, 1993; Johannes et al., 1994; Hammouda et al., 1996; Nakamura and Shimakita, 1998), and that NaSi-CaAl diffusion is too slow to exert major control on dissolution kinetics (cf. Liu and Yund, 1992). Our experimental textures are consistent with this model of congruent melting and recrystallisation. Considering the slow intracrystalline NaSi-CaAl diffusion rates, it is also considered unlikely that diffusion could have produced the larger compositional variability of the plagioclase cores in our resorption experiments compared to the 870°C baseline experiment (Fig. 5d; Table 1). Instead, we posit that more anorthitic domains in crystal interiors are generally related to dissolution and recrystallisation of a more calcic plagioclase at elevated temperatures, similar to crystal rims. This interpretation is supported by the observation that more anorthitic domains are often associated with melt inclusions (Fig. 6b & c).

Rapid recrystallisation during cooling does not change crystal shape

Temperature cycling experiment 23-CSB-05 provides insight into growth processes upon cooling from 900°C to 870°C. The <2 µm, An-rich rims crystallised at 900°C are now overgrown by mantles, which measure 1-50 µm in width and constitute some 60% of the total

area crystallinity. Proximal to the high-An plagioclase bands, the mantles contain abundant melt inclusions (2 to >10 μm in size) and occasionally show complex, diffuse textures (Fig. 9a, Fig. 11c) characterised by small but significant differences in An content (ΔAn ≤5 mol % within the mantle; Pl_{1b} in Fig. 11c); towards the rims of the crystals, compositions then approximate those of the crystal cores grown at 870°C (Pl_2 in Fig 11c).

The experimental melt inclusions are commonly found in close association with embayed crystal core topographies (Figs. 9b & 11c), indicating that they were necked off during rapid growth (cf. Nakamura and Shimakita, 1998). We therefore suggest that plagioclase mantles grew rapidly upon cooling from 900°C to 870°C. High growth rates are interpreted to be a combined result of the rapid cooling (30°C in 15 minutes) and the interface roughness of the dissolution surface, which could facilitate a continuous growth mechanism due to the high density of kinks and steps (Jackson et al., 1967; Kirkpatrick, 1975; Sunagawa, 2007). The initial textural and compositional heterogeneity of the mantles also reflects rapid growth: the boundary layer melt (M_1 in Fig. 11) at 900°C is compositionally heterogeneous due to supply of resorbed plagioclase components and simultaneous diffusion into the melt (see above), and this melt heterogeneity will be preserved in the crystals if growth is faster than melt diffusion. Consistently, the melt inclusions trapped in the plagioclase mantle cover the same range in compositions as the boundary layer melt at 900°C (23-CSB-03), with Ca/Na ratios considerably higher (average $CaO/Na_2O = 0.7$) and more variable ($CaO/Na_2O = 0.3$-1.2) than those typical for far-field glass (Table 1; Supplementary Material S1.2). Nakamura and Shimakita (1998) have previously described the dissolution and entrapment origin of many melt inclusions, which constitutes an important petrogenetic counterpart to the melt inclusions trapped during rapid skeletal growth (Kohut and Nielsen, 2004; Faure and Schiano, 2005; Bennett et al., 2019). Our results provide additional experimental evidence for a dissolution origin of melt inclusions and emphasise that adequate interpretation of melt

inclusion data critically depend on a thorough understanding of how the inclusions formed. The results of this study further highlight the challenging nature of using crystal textures for petrogenetic interpretations: the textures produced by a simple temperature fluctuation of 30°C over the course of two weeks at magmatic conditions are highly complex. We suggest that many petrologists would not have ascribed the presence of patchy zoning (Fig. 9a) or multiple apparent dissolution fronts (Fig. 9c) to such a simple heating event. Crystal sectioning effects play a crucial role in further complicating the interpretation of already complex textural features.

With respect to crystal morphologies resulting from growth during cooling to 870°C, it is of note that average plagioclase shapes (S/I = 0.28 ± 0.04) are identical to those observed in the experiment that was quenched directly from 900°C (S/I = 0.28 ± 0.04) and slightly less tabular than crystals grown at 870°C (S/I = 0.24 ± 0.03; Fig. 8b). While this difference between plagioclase shapes in the static and cycled experiments is subtle and likely sensitive to the exact experimental conditions, it nonetheless suggests that overgrowth of resorbed cores does not re-establish original crystal morphologies but instead preserves the aspect ratios of the resorbed cores. In the experiments, the aspect ratios of the overgrowth mantles themselves could not be robustly determined due to an insufficient number of appropriate 2D sections, precluding further investigation of this observation. However, this will be addressed below using the shapes of overgrowth mantles on MSH plagioclase crystals.

Comparison to Mount St. Helens plagioclase textures

Samples in the Mount St. Helens plagioclase shape database

We compared experimental crystal textures to those of plagioclase crystals in a range of volcanic rocks from Mount St. Helens. The sample suite (Table 2; Figs. 12 & 13) consists of a 1982 dome dacite, a Castle Creek age basalt, three mush inclusions and three quenched magmatic inclusions (QMI) hosted in dacites of the Spirit Lake stage (<4 ka BP; Clynne et

al., 2008; Pallister et al., 2008). Major and trace element compositions of the studied plagioclase crystals are typical for the MSH plumbing system and do not belong to older Tertiary intrusions (Fig. 12; Supplementary Material S2.2; Kent et al., 2008; Schlieder et al., 2022). The Castle Creek age basalt represents one of several mafic inputs into the MSH plumbing system (Wanke et al., 2019a) and contains predominantly small (l_{av} = 71 µm; Table 2), unresorbed plagioclase crystals indicative of a simple crystallisation history (Fig. 13a). Rare QMIs are evidence for interaction between mafic and evolved magmas and they are characterised by diktytaxitic textures dominated by unresorbed plagioclase (Fig. 13b). Diktytaxitic textures are the result of rapid crystallisation due to undercooling of the mafic magma upon injection into the host dacite (Pallister et al., 2008). The range in crystal sizes observed in QMIs (l_{av} = 96-161 µm; Table 2) suggests variable cooling rates, and up to 37% of crystals show surficial resorption, indicating a more complex growth history. Besides QMIs, MSH dacites carry inclusions of coarser, crystal-rich material consisting of resorbed plagioclase, amphibole, and orthopyroxene. Such inclusions and glomerocrysts have been interpreted as cognate crystal mush entrained at depth during magma ascent (Wanke et al., 2019a), in which case they would offer a direct window into crystal storage conditions at MSH. Plagioclase in mush inclusions are larger in size (l_{av} = 225-356 µm; Table 2) and almost universally affected by one or multiple surficial or pervasive resorptions events (Fig. 13c). The 1982 dacite represents a typical hybridised magma with a heterogeneous crystal cargo sampling multiple crystallisation environments and histories (Streck et al., 2008; Cashman and Blundy, 2013). Plagioclase in the dome dacite show a range of textures reflecting this diversity: 16% of crystals are unresorbed, 39% show one or several surficial dissolution surfaces, and 45% show additional evidence for pervasive resorption (Fig. 13d; Table 2). In the following section, we examine the textural characteristics of the MSH plagioclase cargo within the framework of our new experiments.

606 ### *Comparison of natural textures with resorption experiments*

607 Several key features of the textures produced during our resorption experiments are common
608 in MSH plagioclase crystals. Most importantly, the majority of plagioclase crystals in MSH
609 dacites show at least one dissolution surface associated with round edges (Fig. 14a & b),
610 similar to some experimental crystals (e.g., Fig. 9a). Moreover, many natural plagioclase
611 crystals exhibit rough dissolution surfaces with irregular topography (Fig. 14a & c), which
612 strikingly resemble textures produced in our heating experiments (Figs. 6, 9 & 10) and are
613 sometimes associated with melt inclusions (Fig. 14a). In addition, there are several instances
614 of resorbed, intergrown crystals with a shared An-rich rim (Fig. 14a & b), which we also
615 observed in experiments (Fig. 10), and which indicates that intergrowth occurred before
616 magmatic cooling post-resorption. Finally, single plagioclase crystals with two distinct
617 resorbed cores are present in MSH rocks (Fig. 14c), which is also a common feature in
618 experimental plagioclase crystals (Fig. 10). Smooth and rough dissolution surfaces in natural
619 crystals are overgrown by An-rich plagioclase, followed by a return to more albitic
620 compositions via normal zoning (Fig. 14; Streck et al., 2008). This is qualitatively consistent
621 with the experimental An-rich bands and lower-An mantles observed in the temperature
622 cycling experiment. Indeed, Streck et al. (2008) suggest that dissolution surfaces in MSH
623 plagioclase crystals reflect temperature fluctuations of ≤45°C and resulting changes in
624 crystallinity of ≤25% during prolonged storage. Our experiments provide additional textural
625 evidence in support of this hypothesis. Within this framework of heating-induced crystal
626 resorption, we note that MSH plagioclase crystals show evidence for multiple heating events
627 (Fig. 14), whereas experimental crystals were only heated once. Since our experiments show
628 that resorption decreases 3D crystal aspect ratios, we use the MSH sample suite to test
629 whether multiple resorption events lead to a greater reduction in aspect ratios.

Plagioclase shape variability at Mount St. Helens

To quantify the effect of resorption on crystal shape in MSH plagioclase, we subdivided crystals into three categories: (1) unresorbed crystals; (2) crystals showing surficial resorption, i.e., crystals with dissolution surfaces and rounded corners but preserved overall core shapes (cf. Fig. 1a); and (3) crystals showing pervasive resorption, i.e., crystals whose original core shapes have been compromised during extensive dissolution (cf. Fig. 1b). We note that while category (3) includes sieved crystals (e.g., Fig. 13d), most crystals in this category do not show sieving but rather highly irregular core surfaces (e.g., Fig. 13c) and patchy interiors (Supplementary Material 2.1).

For the 1982 dome dacite, crystal textures were sufficiently diverse to constrain shapes for all three categories; plagioclase crystals from all other samples show less textural variability and only fall into one or two of the three resorption categories (Table 2; Fig. 15). In Fig. 15a, representative crystal shapes for each resorption category across all samples are shown. Unresorbed plagioclase crystals have tabular shapes (S/I = 0.27-0.37; Table 2; blue symbols in Fig. 15), whereas resorbed crystals are more equant, with surficial resorption producing a large range of aspect ratios (S/I = 0.33 – 0.63; lavender symbols in Fig. 15) and pervasive resorption resulting in the most compact, low-aspect-ratio shapes (S/I = 0.56 – 0.71; Table 2; purple symbols in Fig. 15). This decrease in 3D crystal aspect ratio during resorption is consistent with our experimental observations. We posit that the greater magnitude of shape change in MSH samples is due to the greater number of resorption-recrystallisation events in response to repeated thermal fluctuations (or other processes inducing disequilibrium, such as an influx of volatiles) over geologically relevant timescales. In addition, the presence of sieve textures in MSH plagioclase suggests that some crystals were exposed to greater degrees of disequilibrium than those imposed in our experiments, which did not produce sieve textures.

654 This implies a larger extent of dissolution and hence a more pronounced reduction in crystal
655 aspect ratios.

656 Notably, unresorbed crystals exhibit similar shapes irrespective of magmatic compositions
657 and crystallisation environment. This indicates that despite the large range of crystallisation
658 conditions for the different samples, relative growth rates of plagioclase along the different
659 growth directions were remarkably similar. Within the framework of Mangler et al. (2023),
660 who modelled relative growth rates as the competition between melt diffusivity and interface
661 reaction kinetics, this implies that the relative rates of melt diffusion and to interface reaction
662 were similar in all cases.

663 In addition to entire crystal morphologies, we separately measured plagioclase core and
664 mantle shapes in the 1982 dome sample to examine the effect of overgrowth on crystal shape
665 in natural samples (Table 2; Fig. 15b). Consistent with our observations in cycling
666 experiment 23-CSB-05, crystal core shapes are consistent with entire crystal shapes
667 irrespective of mantle shapes. For example, plagioclase crystals with surficial resorption
668 textures have tabular cores (S/I = 0.43) and tabular overall shapes (S/I = 0.45), yet their
669 mantles are significantly more equant (S/I = 0.57). This observation may be explained by the
670 crystal growth model of Mangler et al. (2022), who found that crystal shapes are insensitive
671 to relatively small overgrowth volumes. Interestingly, mantles of both surficially and
672 pervasively resorbed crystals have similar growth shapes (S/I = 0.57 – 0.67), and they are
673 more equant than primary growth shapes (represented by unresorbed crystals, S/I = 0.33).
674 This suggests that relative growth rates along different crystallographic directions were more
675 similar during mantle crystallisation than those during primary growth. This points towards
676 different growth mechanisms. Indeed, the rough surfaces of the resorbed crystals would
677 favour continuous growth over layer growth mechanisms (i.e., spiral or surface nucleation
678 growth), which dominate at smooth interfaces (Kirkpatrick, 1975; Lasaga, 1998). Continuous

679 growth is driven by a high density of kinks and steps on the crystal surface rather than by
680 variations in surface energy on different crystal faces (Hartman and Perdok, 1955; Jackson et
681 al., 1967; Kirkpatrick, 1975). Therefore, a change from layer growth to continuous growth,
682 caused by resorption, could explain the lower aspect ratios (i.e., high *S/I*) of the plagioclase
683 mantles. Alternatively, it is also possible that relative overgrowth rates are different from
684 primary growth due to the larger sizes of resorbed crystals compared to nuclei, as growth
685 kinetics are known to be size dependent (e.g., Eberl et al., 2002; Gaidies and George, 2021).
686 The relationship between resorption and 3D crystal aspect ratio, demonstrated both
687 experimentally and in samples from MSH, implies that the shapes of plagioclase crystals in a
688 magma reservoir will become less tabular every time they are remobilised and resorbed. In
689 the final section, we discuss the effect of this maturation on mush properties and plumbing
690 system dynamics.

691 ### *Maturation of a crystal mush and its effect on mush eruptibility*

692 Current models of crustal magma storage envisage trans-crustal plumbing systems with large
693 regions of crystal mush (i.e., a rigid framework of interlocking crystals with interstitial melt)
694 potentially hosting smaller and transient domains of liquid-dominated, eruptible magmas
695 (Annen et al., 2015; Cashman et al., 2017; Cooper, 2019). In this framework, the crystal
696 cargo erupted at volcanoes across tectonic settings is considered to be at least partly derived
697 from remobilised and disaggregated crystal mushes, which is consistent with heterogeneous
698 crystallisation ages, textures and compositions of co-erupted crystals (e.g., Charlier et al.,
699 2005; Davidson et al., 2007; Cooper and Donnelly, 2008; Passmore et al., 2012; Cashman
700 and Blundy, 2013; Evans and Bachmann, 2013; Wolff et al. 2015; Humphreys et al., 2019;
701 Mangler et al., 2020; Schlieder et al., 2022). For example, plagioclase crystals erupted at
702 MSH in 1980-86 and 2004-05 show U-series crystallisation ages ranging from >20-40 ka to
703 zero-age (Cooper and Reid, 2003; Cooper and Donnely, 2008; Schlieder et al., 2022), and

Schlieder et al. (2022) used Sr diffusion in plagioclase to show that a significant fraction of these crystals spent >95% of their storage in a crystal mush ("cold storage", e.g. Cooper and Kent, 2014). The diversity of erupted MSH plagioclase textures is consistent with this view and highlights the heterogeneity of the MSH plumbing system: any erupted crystal has a unique crystallisation and remobilisation history, depending on their pathway through the distinct magmatic environments in the plumbing system. Resorption textures in MSH plagioclase record mush disaggregation and reformation processes, and we can use the observed plagioclase diversity to exemplify the textural evolution of a crystal mush as it forms and matures, i.e., as it is repeatedly remobilised and subject to resorption (Fig. 16). Upon ascent and emplacement of a new melt batch in the crust (step (0) in Fig. 16), tabular plagioclase will crystallise. Due to the high aspect ratios of the crystals, the maximum packing fraction (i.e., rheological lockup) will be reached at relatively high temperatures (T_{lockup} in Fig. 16) and low crystallinities, and an interlocking crystal network will form (i.e., a mush; blue in Fig. 16). We suggest that such immature mush textures and crystal shapes will resemble those of the quenched magmatic inclusions at MSH (Fig. 13b). Crystals will then be stored at temperatures close to the solidus for various amounts of time (years to >10 kys; Schlieder et al., 2022) before being rejuvenated by a renewed influx of magma, volatiles, or heat. Upon rejuvenation of the primary mush, interlocking crystal networks will be disaggregated, and individual crystals resorbed, which will result in more equant crystal shapes with lower aspect ratios (step (1) in Fig. 16). Cooling and recrystallisation after the remobilisation event will re-establish a texturally more mature crystal mush, which will form at slightly higher crystallinities and lower T_{lockup}. Each subsequent remobilisation and resorption event will advance mush maturation by further reducing crystal aspect ratios and hence T_{lockup} (step (2) in Fig. 16). The crystal cargoes in the mush enclave samples (Fig. 13c) and the 1982 dacite (Fig. 13d) show various stages of crystal maturation.

729 Crystal mush maturation has important effects on its rheological properties. Mader et al.
730 (2013) describe maximum packing fractions of magmas as a function of crystal shape. The
731 aspect ratios of MSH plagioclase categories (Table 2) can be used to estimate how lock-up
732 crystallinities change during mush maturation: Primary, unresorbed, tabular MSH plagioclase
733 (S/I ~ 0.3) has a lock-up crystallinity of ~40%, whereas mature, equant, resorbed plagioclase
734 (S/I ~ 0.7) locks up at ~50% (Fig. 16). This difference in lock-up crystallinities prescribes
735 that a mature crystal mush becomes rheologically locked at lower temperatures than an
736 immature mush: R-MELTS modelling (Gualda and Ghiorso, 2015) suggests ~35°C
737 difference between 40% and 50% crystallinity for a water-saturated MSH dacite (Riker et al.,
738 2015) at 200 MPa. This means that as a crystal mush matures, it remains rheologically mobile
739 – and hence eruptible – for longer (orange in Fig. 16), and it can also be remobilised more
740 easily.

741 The above model, and the experiments upon which it is based, are simplifications in several
742 aspects. Firstly, it assumes that resorption is exclusively related to thermal fluctuations, even
743 though it is well known that changes in melt composition, volatile content, oxygen fugacity,
744 and pressure can equally destabilise mineral phases and drive resorption. Similarly, our
745 experiments studied plagioclase in a near-liquidus melt, but a natural mush is, by definition,
746 crystal-rich, and will comprise several mineral phases. Despite these caveats, our experiments
747 reproduced surficial resorption textures typical for MSH (Figs. 1a & 14) and volcanic rocks
748 in general. This indicates that the experiments approximated typical degrees of disequilibrium
749 in volcanic plumbing systems, irrespective of the exact circumstances and driving forces
750 behind it. We therefore suggest that our findings and interpretation are relevant to resorption-
751 recrystallisation processes in general.

752 Secondly, the model assumes that every crystal in a given mush domain will be equally
753 affected by perturbations. In reality, not every crystal will be affected by every remobilisation

event, depending on its position in the mush pile (e.g., Cheng et al., 2020; Platt et al., 2023). Similarly, some crystals may experience little or no resorption during remobilisation (as seen in our experiments), while others may be subject to pervasive resorption (depending on its individual exposure to disequilibrium), which would alter their shapes more severely. In addition, magma recharge will periodically introduce additional, less mature crystals from depth. Hence, any crystal mush with a history of multiple remobilisation events will exhibit a diverse crystal cargo of varying maturity (i.e., variable crystal shapes), which will affect magma rheology (Moitra and Gonnerman, 2015).

Thirdly, in complex plumbing systems such as MSH, there are several mush environments at distinct depths and temperatures, with distinct compositions, phase assemblages, and remobilisation histories, and hence different degrees of maturity (Wanke et al., 2019a &b; Schlieder et al., 2022; Keller et al., 2024).

Nonetheless, our study demonstrates that mature volcanic plumbing systems such as MSH are dominated by mush with more equant crystals, whereas immature plumbing systems are likely characterised by mush with a higher abundance of tabular crystals. This has important implications for the dynamics and timescales of pre-eruptive magma assembly. A mature mush can produce eruptible magmas on shorter timescales and with less mass, volatile, or heat input than an immature mush. Large eruptions resulting from wholesale remobilisation of mushy reservoirs are therefore more likely to occur in thermally more mature plumbing systems. Moreover, since mush permeability is also a function of crystal shape (Bretagne et al., 2023), a mature mush likely has a higher permeability than an immature mush. This may facilitate melt extraction and hence formation of large volumes of eruptible crystal-poor rhyolite (Liu and Lee, 2021). On the other hand, higher mush permeability can also facilitate reservoir outgassing through magmatic volatile phase channels in the mush (Parmigiani et al., 2011; Oppenheimer et al., 2015), which affects magma reservoir compressibility and hence

779 eruption rates, durations, and styles (Huppert and Woods, 2002; Degruyter et al., 2017;
780 2019). Mush maturation may therefore be an important aspect of the thermal maturation of
781 magmatic plumbing systems, which is known to facilitate larger eruptions (e.g., de Silva and
782 Gosnold, 2007; Walker et al., 2010). This shows that studies into crystal shape inventories
783 and hence maturity of magmatic systems have great potential to improve our understanding
784 of mush remobilisation and pre-eruptive magma dynamics and timescales.

785 Conclusions

786 We provide experimental evidence that temperature fluctuations of 20-40°C can reproduce
787 resorption textures typical for plagioclase crystals in MSH rocks and many other arc
788 volcanoes worldwide. Resorption results in a reduction of 3D aspect ratios of experimental
789 plagioclase crystals, and the same observation that resorbed crystals are more equant is also
790 true for MSH plagioclase. Our findings suggest that the shapes of plagioclase crystals in a
791 magma reservoir will become less tabular every time they are remobilised and resorbed.
792 More generally, the crystal cargo of a mush stored in the crust will become more equant as it
793 matures, i.e., over the course of repeated cycles of resorption and recrystallisation. Since
794 crystal shape affects the crystallinities and temperatures at which a crystal mush unlocks and
795 becomes eruptible, mature mushes can be remobilised and erupted more easily and over
796 shorter timescales than immature mushes dominated by unresorbed, tabular shapes.

797 Funding

798 This work was funded by UK Natural Environment Research Council grant NE/T000430/1.
799 This project has received funding from the European Research Council (ERC) under the
800 European Union's Horizon 2020 research and innovation programme (grant agreement No.
801 864923). AAI acknowledges support from The Leverhulme Trust through an Early Career
802 Fellowship.

Acknowledgments

We are grateful to Jenni Barclay for donating her cold-seal pressure vessel setup. We thank Leon Bowen of the GJ Russell Electron Microscopy Facility at Durham University for facilitating SEM imaging and analysis, Chris Hayward for assistance with EPMA analysis, and Chris Ottley for facilitating LA-ICP-MS analysis. We further thank Heather Wright for assistance during fieldwork at Mount St. Helens, and Cathrine Annen, Charline Lormand as well as the mush discussion group at Durham University for fruitful conversations about crystal mush processes. We thank Julia Hammer, Dawnika Blatter, Fabio Arzilli, and an anonymous reviewer, as well as associate editor Adam Kent, for their comments, which helped improve this work.

Data Availability

The data underlying this article are available in its online supplementary material.

References

Allègre, C. J., Provost, A., & Jaupart, C. (1981). Oscillatory zoning: a pathological case of crystal growth. *Nature*, 294(5838), 223-228. doi: 10.1038/294223a0

Anderson, A. T. (1984). Probable relations between plagioclase zoning and magma dynamics, Fuego Volcano, Guatemala. *American Mineralogist*, 69(7-8), 660-676.

Annen, C., Blundy, J. D., Leuthold, J., & Sparks, R. S. J. (2015). Construction and evolution of igneous bodies: Towards an integrated perspective of crustal magmatism. *Lithos*, 230, 206-221. doi: 10.1016/j.lithos.2015.05.008

826 Arvidson, R. S., Ertan, I. E., Amonette, J. E., & Lüttge, A. (2003). Variation in calcite
827 dissolution rates:: A fundamental problem?. *Geochimica et Cosmochimica Acta*, *67*(9), 1623-
828 1634. doi: 10.1016/S0016-7037(02)01177-8

829 Arzilli, F., Polacci, M., La Spina, G., Le Gall, N., Llewellin, E. W., Brooker, R. A., ... &
830 Burton, M. R. (2022). Dendritic crystallization in hydrous basaltic magmas controls magma
831 mobility within the Earth's crust. *Nature Communications*, 13(1), 3354. doi: 10.1038/s41467-
832 022-30890-8

833 Bachmann, O., & Bergantz, G. W. (2006). Gas percolation in upper-crustal silicic crystal
834 mushes as a mechanism for upward heat advection and rejuvenation of near-solidus magma
835 bodies. *Journal of Volcanology and Geothermal research*, 149(1-2), 85-102. Doi:
836 10.1016/j.jvolgeores.2005.06.002

837 Bennett, E. N., Lissenberg, C. J., & Cashman, K. V. (2019). The significance of plagioclase
838 textures in mid-ocean ridge basalt (Gakkel Ridge, Arctic Ocean). *Contributions to*
839 *Mineralogy and Petrology*, 174, 1-22. Doi: 10.1007/s00410-019-1587-1

840 Berlo, K., Blundy, J., Turner, S., & Hawkesworth, C. (2007). Textural and chemical variation
841 in plagioclase phenocrysts from the 1980 eruptions of Mount St. Helens, USA. *Contributions*
842 *to Mineralogy and Petrology*, 154, 291-308. Doi: 10.1007/s00410-007-0194-8

843 Blatter, D. L., Sisson, T. W., & Hankins, W. B. (2017). Voluminous arc dacites as amphibole
844 reaction-boundary liquids. *Contributions to Mineralogy and Petrology*, *172*, 1-37. doi:
845 10.1007/s00410-017-1340-6

846 Blum, A. E., & Lasaga, A. C. (1987). Monte Carlo simulations of surface reaction rate
847 laws. *IN: Aquatic Surface Chemistry: Chemical Processes at the Particle-Water Interface.*
848 *John Wiley and Sons, New York*, 255-292.

849 Boulanger, M., & France, L. (2023). Cumulate formation and melt extraction from mush-
850 dominated magma reservoirs: the melt flush process exemplified at mid-ocean
851 ridges. *Journal of Petrology*, *64*(2), egad005.

852 Brugger, C. R., & Hammer, J. E. (2015). Prevalence of growth twins among anhedral
853 plagioclase microlites. *American Mineralogist*, 100(2-3), 385-395. doi: 10.2138/am-2015-
854 4809

855 Caricchi, L., Burlini, L., Ulmer, P., Gerya, T., Vassalli, M., & Papale, P. (2007). Non-
856 Newtonian rheology of crystal-bearing magmas and implications for magma ascent

dynamics. *Earth and Planetary Science Letters*, 264(3-4), 402-419. doi: 10.1016/j.epsl.2007.09.032

Cashman, K., & Blundy, J. (2013). Petrological cannibalism: the chemical and textural consequences of incremental magma body growth. *Contributions to Mineralogy and Petrology*, 166, 703-729. doi: 10.1007/s00410-013-0895-0

Cashman, K. V., Sparks, R. S. J., & Blundy, J. D. (2017). Vertically extensive and unstable magmatic systems: a unified view of igneous processes. *Science*, *355*(6331), eaag3055. doi: 10.1126/science.aag3055

Castro, A. (2001). Plagioclase morphologies in assimilation experiments. Implications for disequilibrium melting in the generation of granodiorite rocks. *Mineralogy and Petrology*, 71, 31-49. doi: 10.1007/s007100170044

Chakraborty, S. (2008). Diffusion in solid silicates: a tool to track timescales of processes comes of age. *Annu. Rev. Earth Planet. Sci.*, 36, 153-190. doi: 10.1146/annurev.earth.36.031207.124125

Charlier, B. L. A., Wilson, C. J. N., Lowenstern, J. B., Blake, S., Van Calsteren, P. W., & Davidson, J. P. (2005). Magma generation at a large, hyperactive silicic volcano (Taupo, New Zealand) revealed by U–Th and U–Pb systematics in zircons. *Journal of Petrology*, 46(1), 3-32. doi: 10.1093/petrology/egh060

Cheng, L., Costa, F., & Bergantz, G. (2020). Linking fluid dynamics and olivine crystal scale zoning during simulated magma intrusion. *Contributions to Mineralogy and Petrology*, *175*, 1-14. doi: 10.1007/s00410-020-01691-3

Chernov, A. A., (1984). *Modern Crystallography III: Crystal Growth*, 48-103.

Claiborne, L. L., Miller, C. F., Flanagan, D. M., Clynne, M. A., & Wooden, J. L. (2010). Zircon reveals protracted magma storage and recycling beneath Mount St. Helens. *Geology*, 38(11), 1011-1014. doi: 10.1130/G31285.1

Clynne, M. A., Calvert, A. T., Wolfe, E. W., Evarts, R. C., Fleck, R. J., Lanphere, M. A., ... & Stauffer, P. H. (2004). The Pleistocene eruptive history of Mount St. Helens, Washington, from 300,000 to 12,800 years before present. *In*: Sherrod D. R., Scott W. E. & Stauffer P. H. (eds) *A Volcano Rekindled: The First Year of Renewed Eruption at Mount St. Helens, 2004–2006*. United States Geological Survey, Professional Paper, 1750, 593-627.

887 Cooper, K. M. (2019). Time scales and temperatures of crystal storage in magma reservoirs:
888 implications for magma reservoir dynamics. *Philosophical Transactions of the Royal Society*
889 *A*, 377(2139), 20180009. doi: 10.1098/rsta.2018.0009

890 Cooper, K. M. & Donnelly, C. T. (2008). ^{238}U–^{230}Th–^{226}Ra Disequilibria in dacite and
891 plagioclase from the 2004–2005 eruption of Mount St. Helens. *In*: Sherrod D. R., Scott W. E.
892 & Stauffer P. H. (eds) *A Volcano Rekindled: The First Year of Renewed Eruption at Mount*
893 *St. Helens, 2004–2006*. United States Geological Survey, Professional Paper, 1750, 827–846.

894 Cooper, K. M., & Kent, A. J. (2014). Rapid remobilization of magmatic crystals kept in cold
895 storage. *Nature*, 506(7489), 480-483. Doi: 10.1038/nature12991

896 Cooper, K. M., & Reid, M. R. (2003). Re-examination of crystal ages in recent Mount St.
897 Helens lavas: implications for magma reservoir processes. *Earth and Planetary Science*
898 *Letters*, 213(1-2), 149-167. doi: 10.1016/S0012-821X(03)00262-0.

899 Couch, S., Sparks, R. S. J., & Carroll, M. R. (2001). Mineral disequilibrium in lavas
900 explained by convective self-mixing in open magma chambers. *Nature, 411*(6841), 1037-
901 1039. doi: 10.1038/35082540

902 Costa, F., Shea, T., & Ubide, T. (2020). Diffusion chronometry and the timescales of
903 magmatic processes. *Nature Reviews Earth & Environment*, 1(4), 201-214. doi:
904 10.1038/s43017-020-0038-x

905 Danyushevsky, L. V. (2001). The effect of small amounts of H2O on crystallisation of mid-
906 ocean ridge and backarc basin magmas. *Journal of Volcanology and Geothermal*
907 *Research*, 110(3-4), 265-280. doi: 10.1016/S0377-0273(01)00213-X

908 Davidson, J. P., Morgan, D. J., Charlier, B. L. A., Harlou, R., & Hora, J. M. (2007).
909 Microsampling and isotopic analysis of igneous rocks: implications for the study of magmatic
910 systems. *Annual Review of Earth and Planetary Sciences*, *35*, 273-311. doi:
911 10.1146/annurev.earth.35.031306.140211

912 Degruyter, W., Huber, C., Bachmann, O., Cooper, K. M., & Kent, A. J. (2017). Influence of
913 exsolved volatiles on reheating silicic magmas by recharge and consequences for eruptive
914 style at Volcán Quizapu (Chile). *Geochemistry, Geophysics, Geosystems*, *18*(11), 4123-4135.
915 doi: 10.1002/2017GC007219

Degruyter, W., Parmigiani, A., Huber, C., & Bachmann, O. (2019). How do volatiles escape their shallow magmatic hearth?. *Philosophical Transactions of the Royal Society A*, *377*(2139), 20180017. doi: 10.1098/rsta.2018.0017

de Silva, S. L., & Gosnold, W. D. (2007). Episodic construction of batholiths: Insights from the spatiotemporal development of an ignimbrite flare-up. *Journal of Volcanology and Geothermal Research*, *167*(1-4), 320-335. doi: j.jvolgeores.2007.07.015

Dohmen, R., Faak, K., & Blundy, J. D. (2017). Chronometry and speedometry of magmatic processes using chemical diffusion in olivine, plagioclase and pyroxenes. *Reviews in Mineralogy and Geochemistry*, 83(1), 535-575. doi: 10.2138/rmg.2017.83.16

Eberl, D. D., Kile, D. E., & Drits, V. A. (2002). On geological interpretations of crystal size distributions: Constant vs. proportionate growth. *American Mineralogist*, 87(8-9), 1235-1241. doi: 10.2138/am-2002-8-923

Erdmann, M., & Koepke, J. (2016). Experimental temperature cycling as a powerful tool to enlarge melt pools and crystals at magma storage conditions. *American Mineralogist*, 101(4), 960-969. doi: 10.2138/am-2016-5398

Evans, B. W., & Bachmann, O. (2013). Implications of equilibrium and disequilibrium among crystal phases in the Bishop Tuff. *American Mineralogist*, 98(1), 271-274. doi: 10.2138/am.2013.4280

Faure, F., & Schiano, P. (2005). Experimental investigation of equilibration conditions during forsterite growth and melt inclusion formation. *Earth and Planetary Science Letters*, 236(3-4), 882-898. doi: 10.1016/j.epsl.2005.04.050

Fischer, C., Arvidson, R. S., & Lüttge, A. (2012). How predictable are dissolution rates of crystalline material?. *Geochimica et Cosmochimica Acta*, 98, 177-185. doi: 10.1016/j.gca.2012.09.011

Fischer, C., Kurganskaya, I., Schäfer, T., & Lüttge, A. (2014). Variability of crystal surface reactivity: what do we know?. *Applied Geochemistry*, 43, 132-157. doi: 10.1016/j.apgeochem.2014.02.002

Fletcher, N. H. (1958). Size effect in heterogeneous nucleation. *The Journal of chemical physics*, 29(3), 572-576.

Gaidies, F., & George, F. R. (2021). The interfacial energy penalty to crystal growth close to equilibrium. *Geology*, 49(8), 988-992. doi: 10.1130/G48715.1

947 Gardner, J. E., Carey, S., Rutherford, M. J., & Sigurdsson, H. (1995). Petrologic diversity in
948 Mount St. Helens dacites during the last 4,000 years: implications for magma
949 mixing. *Contributions to Mineralogy and Petrology*, *119*, 224-238. doi:
950 10.1007/BF00307283

951 Gardner, J. E., Rutherford, M., Carey, S., & Sigurdsson, H. (1995). Experimental constraints
952 on pre-eruptive water contents and changing magma storage prior to explosive eruptions of
953 Mount St Helens volcano. *Bulletin of Volcanology*, *57*, 1-17. doi: 10.1007/BF00298703

954 Gelman, S. E., Gutiérrez, F. J., & Bachmann, O. (2013). On the longevity of large upper
955 crustal silicic magma reservoirs. *Geology*, 41(7), 759-762. doi: 10.1130/G34241.1

956 Geschwind, C. H., & Rutherford, M. J. (1992). Cummingtonite and the evolution of the
957 Mount St. Helens (Washington) magma system: an experimental study. *Geology*, *20*(11),
958 1011-1014. doi: 10.1130/0091-7613(1992)020%3C1011:CATEOT%3E2.3.CO;2

959 Gibbs, J. W. (1878). On the equilibrium of heterogeneous substances. *American Journal of*
960 *Science*, *3*(96), 441-458.

961 Ginibre, C., Kronz, A., & Wörner, G. (2002). High-resolution quantitative imaging of
962 plagioclase composition using accumulated backscattered electron images: new constraints
963 on oscillatory zoning. *Contributions to Mineralogy and Petrology*, *142*(4), 436-448. doi:
964 10.1007/s004100100298

965 Ginibre, C., Wörner, G., & Kronz, A. (2007). Crystal zoning as an archive for magma
966 evolution. *Elements*, 3(4), 261-266. doi: 10.2113/gselements.3.4.261

967 Giuliani, L., Iezzi, G., Vetere, F., Behrens, H., Mollo, S., Cauti, F., ... & Scarlato, P. (2020).
968 Evolution of textures, crystal size distributions and growth rates of plagioclase,
969 clinopyroxene and spinel crystallized at variable cooling rates from a mid-ocean ridge
970 basaltic melt. *Earth-Science Reviews*, 204, 103165. doi: 10.1016/j.earscirev.2020.103165

971 Grove, T. L., Baker, M. B. & Kinzler, R. J. (1984). Coupled CaAl-NaSi diffusion in
972 plagioclase feldspar: experiments and applications to cooling rate speedometry. *Geochim.*
973 *Cosmochim. Acta*, 48(10), 2113–2121. doi: 10.1016/0016-7037(84)90391-0

974 Gualda, G.A.R. & Ghiorso, M.S. (2015). MELTS_Excel: A Microsoft Excel-based MELTS
975 interface for research and teaching of magma properties and evolution. *Geochemistry,*
976 *Geophysics, Geosystems,* 16(1), 315-324. doi: 10.1002/2014GC005545

977 Hammer, J.E. & Rutherford, M.J. (2002). An experimental study of the kinetics of
978 decompression-induced crystallization in silicic melt. *Journal of Geophysical Research: Solid*
979 *Earth*, 107(B1), ECV 8-1-ECV 8-24. doi:10.1029/2001jb000281

980 Hammouda, T., Pichavant, M., & Chaussidon, M. (1996). Isotopic equilibration during partial
981 melting: an experimental test of the behaviour of Sr. *Earth and Planetary Science*
982 *Letters*, 144(1-2), 109-121. doi: 10.1016/0012-821X(96)00144-6

983 Hartman, P., & Perdok, W.G. (1955). On the relation between structure and morphology of
984 crystals, *Acta Crystallographica*, 8(1), 49–52, 521–4, 525–9

985 Higgins, M.D. (2000). Measurement of crystal size distributions. *American Mineralogist*,
986 85(9),1105-1116. doi:10.2138/am-2000-8-901

987 Huber, C., Bachmann, O., & Dufek, J. (2011). Thermo-mechanical reactivation of locked
988 crystal mushes: Melting-induced internal fracturing and assimilation processes in
989 magmas. *Earth and Planetary Science Letters*, 304(3-4), 443-454. doi:
990 10.1016/j.epsl.2011.02.022

991 Humphreys, M. C., Cooper, G. F., Zhang, J., Loewen, M., Kent, A. J., Macpherson, C. G., &
992 Davidson, J. P. (2019). Unravelling the complexity of magma plumbing at Mount St. Helens:
993 a new trace element partitioning scheme for amphibole. *Contributions to Mineralogy and*
994 *Petrology*, 174, 1-15. doi: 10.1007/s00410-018-1543-5

995 Huppert, H. E., & Woods, A. W. (2002). The role of volatiles in magma chamber
996 dynamics. *Nature*, *420*(6915), 493-495. doi: 10.1038/nature01211

997 Jackson, K. A. (1958). Growth and Perfection of Crystals. Doremus et al.,Wiley, New York,
998 p. 319.

999 Jackson, K. A., Uhlmann, D. R., & Hunt, J. D. (1967). On the nature of crystal growth from
1000 the melt. *Journal of Crystal Growth*, 1(1), 1-36.

1001 Johannes, W., Koepke, J., & Behrens, H. (1994). Partial melting reactions of plagioclases and
1002 plagioclase-bearing systems. *Feldspars and their reactions*, 161-194.

1003 Keller, F., Wanke, M., Kueter, N., Guillong, M., & Bachmann, O. (2024). An amphibole
1004 perspective on the recent magmatic evolution of Mount St. Helens. *Journal of*
1005 *Petrology*, *65*(01), egad093. doi: 10.1093/petrology/egad093

1006 Kent, A. J., Rowe, M. C., Thornber, C. R., & Pallister, J. S. (2008). Trace element and Pb
1007 isotope composition of plagioclase from dome samples from the 2004–2005 eruption of

Mount St. Helens, Washington. *In*: Sherrod D. R., Scott W. E. & Stauffer P. H. (eds) *A Volcano Rekindled: The First Year of Renewed Eruption at Mount St. Helens, 2004–2006*. United States Geological Survey, Professional Paper, 1750, 809-826.

Kirkpatrick, R. J. (1975). Crystal growth from the melt: a review. *American Mineralogist: Journal of Earth and Planetary Materials*, 60(9-10), 798-814.

Kohut, E. J., & Nielsen, R. L. (2003). Low-pressure phase equilibria of anhydrous anorthite-bearing mafic magmas. *Geochemistry, Geophysics, Geosystems*, 4(7). doi: 10.1029/2002GC000451

Kohut, E., Nielsen, R.L. Melt inclusion formation mechanisms and compositional effects in high-An feldspar and high-Fo olivine in anhydrous mafic silicate liquids. *Contributions to Mineralogy and Petrology*, 147, 684–704 (2004). doi: 10.1007/s00410-004-0576-0

Kossel, W. (1927). Zur Theorie des Kristallwachstums. *Nachrichten von der Gesellschaft der Wissenschaften zu Göttingen, Mathematisch-Physikalische Klasse, 1927*, 135-143.

Lasaga, A. C. (1998). *Kinetic theory in the earth sciences*. Princeton university press.

Lasaga, A. C., & Lüttge, A. (2001). Variation of crystal dissolution rate based on a dissolution stepwave model. *Science*, 291(5512), 2400-2404. doi: 10.1126/science.1058173

Lasaga, A. C., & Lüttge, A. (2004). Mineralogical approaches to fundamental crystal dissolution kinetics. *American Mineralogist*, 89(4), 527-540. doi: 10.2138/am-2004-0407

Lejeune, A. M., & Richet, P. (1995). Rheology of crystal-bearing silicate melts: An experimental study at high viscosities. *Journal of Geophysical Research: Solid Earth*, 100(B3), 4215-4229. doi: 10.1029/94JB02985

L'Heureux, I., & Fowler, A. D. (1996). Dynamical model of oscillatory zoning in plagioclase with nonlinear partition relation. *Geophysical Research Letters*, 23(1), 17-20. doi: 10.1029/95GL03327

Liu, X. Y. (2002). Effect of foreign particles: a comprehensive understanding of 3D heterogeneous nucleation. *Journal of crystal growth*, 237, 1806-1812.

Liu, M., & Yund, R. A. (1992). NaSi-CaAl interdiffusion in plagioclase. *American Mineralogist*, 77(3-4), 275-283.

Liu, B., & Lee, C. T. (2021). Fast melt expulsion from crystal-rich mushes via induced anisotropic permeability. *Earth and Planetary Science Letters*, *571*, 117113. doi: 10.1016/j.epsl.2021.117113

Lofgren, G. (1974). An experimental study of plagioclase crystal morphology; isothermal crystallization. *American Journal of Science*, 274(3), 243-273. doi:10.2475/ajs.274.3.243

Lofgren, G. (1980). Experimental studies on the dynamic crystallization of silicate melts. *In:* Hargreaves, R.B. (ed.) *Physics of magmatic processes*, 487, 551.

Lofgren, G. E., & Norris, P. N. (1981). Experimental duplication of plagioclase sieve and overgrowth textures. In *Geol Soc Am Abstr Progr* (Vol. 498).

Lüttge, A. (2005). Etch pit coalescence, surface area, and overall mineral dissolution rates. *American Mineralogist*, 90(11-12), 1776-1783. doi: 10.2138/am.2005.1734

Mader, H. M., Llewellin, E. W., & Mueller, S. P. (2013). The rheology of two-phase magmas: A review and analysis. *Journal of Volcanology and geothermal Research*, 257, 135-158. doi: 10.1016/j.jvolgeores.2013.02.014

Mangler, M. F., Petrone, C. M., Hill, S., Delgado-Granados, H., & Prytulak, J. (2020). A pyroxenic view on magma hybridization and crystallization at Popocatépetl volcano, Mexico. *Frontiers in Earth Science*, 8, 362. doi: 10.3389/feart.2020.00362

Mangler, M.F., Humphreys, M.C.S., Wadsworth, F.B., Iveson, A.A. & Higgins, M.D. (2022). Variation of plagioclase shape with size in intermediate magmas: a window into incipient plagioclase crystallisation. *Contributions to Mineralogy and Petrology*, 177, 64. doi: 10.1007/s00410-022-01922-9

Mangler, M. F., Humphreys, M. C., Geifman, E., Iveson, A. A., Wadsworth, F. B., Brooker, R. A., ... & Hammond, K. (2023). Melt diffusion-moderated crystal growth and its effect on euhedral crystal shapes. *Journal of Petrology*, 64(8), egad054. doi: 10.1093/petrology/egad054

Martel, C., & Schmidt, B. C. (2003). Decompression experiments as an insight into ascent rates of silicic magmas. *Contributions to Mineralogy and Petrology*, 144(4), 397-415. doi: 10.1007/s00410-002-0404-3

Mills, R. D., & Glazner, A. F. (2013). Experimental study on the effects of temperature cycling on coarsening of plagioclase and olivine in an alkali basalt. *Contributions to Mineralogy and Petrology*, 166, 97-111. doi: 10.1007/s00410-013-0867-4

Moitra, P., & Gonnermann, H. M. (2015). Effects of crystal shape-and size-modality on magma rheology. *Geochemistry, Geophysics, Geosystems*, 16(1), 1-26. doi: 10.1002/2014GC005554

Mueller, S., Llewellin, E. W., & Mader, H. M. (2010). The rheology of suspensions of solid particles. *Proceedings of the Royal Society A: Mathematical, Physical and Engineering Sciences*, 466(2116), 1201-1228. doi: 10.1098/rspa.2009.0445

Mueller, S., Llewellin, E. W., & Mader, H. M. (2011). The effect of particle shape on suspension viscosity and implications for magmatic flows. *Geophysical Research Letters*, 38(13). doi: 10.1029/2011GL047167

Nakamura, M., & Shimakita, S. (1998). Dissolution origin and syn-entrapment compositional change of melt inclusion in plagioclase. *Earth and Planetary Science Letters*, 161(1-4), 119-133. doi: 10.1016/S0012-821X(98)00144-7

Nelson, S. T., & Montana, A. (1992). Sieve-textured plagioclase in volcanic rocks produced by rapid decompression. *American Mineralogist*, 77(11-12), 1242-1249.

Noiriel, C., Oursin, M., Saldi, G., & Haberthür, D. (2019). Direct determination of dissolution rates at crystal surfaces using 3D X-ray microtomography. *ACS Earth and Space Chemistry*, 3(1), 100-108. doi: 10.1021/acsearthspacechem.8b00143

Noiriel, C., Oursin, M., & Daval, D. (2020). Examination of crystal dissolution in 3D: A way to reconcile dissolution rates in the laboratory?. *Geochimica et Cosmochimica Acta*, 273, 1-25. doi: 10.1016/j.gca.2020.01.003

Oppenheimer, J., Rust, A. C., Cashman, K. V., & Sandnes, B. (2015). Gas migration regimes and outgassing in particle-rich suspensions. *Frontiers in Physics*, *3*, 60. doi: 10.3389/fphy.2015.00060

Pallister, J. S., Thornber, C. R., Cashman, K. V., Clynne, M. A., Lowers, H. A., Mandeville, C. W., ... & Stauffer, P. H. (2008). Petrology of the 2004–2006 Mount St. Helens lava dome—implications for magmatic plumbing and eruption triggering. *In*: Sherrod D. R., Scott W. E. & Stauffer P. H. (eds) *A Volcano Rekindled: The First Year of Renewed Eruption at Mount St. Helens, 2004–2006*. United States Geological Survey, Professional Paper, 1750, 647–702.

Panjasawatwong, Y., Danyushevsky, L. V., Crawford, A. J., & Harris, K. L. (1995). An experimental study of the effects of melt composition on plagioclase-melt equilibria at 5 and

10 kbar: implications for the origin of magmatic high-An plagioclase. *Contributions to Mineralogy and Petrology*, 118, 420-432. doi: 10.1007/s004100050024

Parmigiani, A., Huber, C., Bachmann, O., & Chopard, B. (2011). Pore-scale mass and reactant transport in multiphase porous media flows. *Journal of Fluid Mechanics*, *686*, 40-76. doi:10.1017/jfm.2011.268

Passmore, E., Maclennan, J., Fitton, G., & Thordarson, T. (2012). Mush disaggregation in basaltic magma chambers: evidence from the AD 1783 Laki eruption. *Journal of Petrology*, 53(12), 2593-2623. doi: 10.1093/petrology/egt049

Pearce, T. H., & Kolisnik, A. M. (1990). Observations of plagioclase zoning using interference imaging. *Earth-Science Reviews*, 29(1-4), 9-26. doi: 10.1016/0012-8252(0)90024-P

Petrone, C. M., & Mangler, M. F. (2021). Elemental Diffusion Chronostratigraphy: Time-Integrated Insights Into the Dynamics of Plumbing Systems. *Crustal Magmatic System Evolution: Anatomy, Architecture, and Physico-Chemical Processes*, 177-193. doi: 10.1002/9781119564485.ch8

Pinard, P. T., Protheroe, A., Holland, J., Burgess, S., & Statham, P. J. (2020). Development and validation of standardless and standards-based X-ray microanalysis. *IOP Conference Series: Materials Science and Engineering* 891(1). doi: 10.1088/1757-899X/891/1/012020

Platt, B., Putirka, K., & Clynne, M.A. (2023). Does arrival of recharge magma control the timing of volcanic eruptions? Evidence from post recharge cooling in eruptions from Brokeoff Volcano, Lassen Volcanic Center, California. *GSA Abstracts with Programs, 5(4)*. doi: 10.1130/abs/2023CD-38734

Pollet-Villard, M., Daval, D., Ackerer, P., Saldi, G. D., Wild, B., Knauss, K. G., & Fritz, B. (2016). Does crystallographic anisotropy prevent the conventional treatment of aqueous mineral reactivity? A case study based on K-feldspar dissolution kinetics. *Geochimica et Cosmochimica Acta*, 190, 294-308. doi: 10.1016/j.gca.2016.07.007

Riker, J. M., Cashman, K. V., Rust, A. C., & Blundy, J. D. (2015). Experimental constraints on plagioclase crystallization during H 2 O-and H 2 O–CO 2-saturated magma decompression. *Journal of Petrology*, 56(10), 1967-1998. doi: 10.1093/petrology/egv059

Rutherford, M. J., & Hill, P. M. (1993). Magma ascent rates from amphibole breakdown: an experimental study applied to the 1980–1986 Mount St. Helens eruptions. *Journal of Geophysical Research: Solid Earth*, 98(B11), 19667-19685. doi: 10.1029/93JB01613

Rutherford, M.J., & Devine, J.D. (2008). Magmatic conditions and processes in the storage zone of the 2004–2006 Mount St. Helens dacite. *In*: Sherrod D. R., Scott W. E. & Stauffer P. H. (eds) *A Volcano Rekindled: The First Year of Renewed Eruption at Mount St. Helens, 2004–2006*. United States Geological Survey, Professional Paper, 1750, 703-726.

Schlieder, T. D., Cooper, K. M., Kent, A. J., Bradshaw, R., & Huber, C. (2022). Thermal Storage Conditions and Origin of Compositional Diversity of Plagioclase Crystals in Magmas from the 1980 and 2004–2005 Eruptions of Mount Saint Helens. *Journal of Petrology*, 63(8), egac064. doi: 10.1093/petrology/egac064

Schneider, C.A., Rasband, W.S. & Eliceiri, K.W. (2012). NIH Image to ImageJ: 25 years of image analysis. *Nature Methods*, 9(7), 671–675. doi: 10.1038/nmeth.2089

Shea, T. & Hammer, J.E. (2013). Kinetics of cooling- and decompression-induced crystallization in hydrous mafic-intermediate magmas. *Journal of Volcanology and Geothermal Research*, 260, 127-145. doi:10.1016/j.jvolgeores.2013.04.018

Sherrod D. R., Scott W. E. & Stauffer P. H. (eds) (2008). *A Volcano Rekindled: The First Year of Renewed Eruption at Mount St. Helens, 2004–2006*. United States Geological Survey, Professional Paper, 1750.

Sisson, T. W., & Grove, T. L. (1993). Experimental investigations of the role of H 2 O in calc-alkaline differentiation and subduction zone magmatism. *Contributions to Mineralogy and Petrology*, 113, 143-166. doi: 10.1007/BF00283225

Stranski, I. N. (1928). Zur Theorie des Kristallwachstums. *Zeitschrift für physikalische Chemie*, *136*(1), 259-278.

Streck, M. J. (2008). Mineral textures and zoning as evidence for open system processes. *Reviews in Mineralogy and Geochemistry*, 69(1), 595-622. doi: 10.2138/rmg.2008.69.15

Streck, M. J., Broderick, C. A., Thornber, C. R., Clynne, M. A., & Pallister, J. S. (2008). Plagioclase populations and zoning in dacite of the 2004–2005 Mount St. Helens eruption: constraints for magma origin and dynamics. *In*: Sherrod D. R., Scott W. E. & Stauffer P. H.

(eds) *A Volcano Rekindled: The First Year of Renewed Eruption at Mount St. Helens, 2004–2006*. United States Geological Survey, Professional Paper, 1750, 791-808.

Sunagawa, I. (2007). *Crystals: growth, morphology, & perfection*. Cambridge University Press.

Snyder, R. C., & Doherty, M. F. (2007). Faceted crystal shape evolution during dissolution or growth. *AIChE journal*, *53*(5), 1337-1348. doi: 10.1002/aic.11132

Tsuchiyama, A., & Takahashi, E. (1983). Melting kinetics of a plagioclase feldspar. *Contributions to Mineralogy and Petrology*, 84, 345-354. doi: 10.1007/BF01160286

Tsuchiyama, A. (1985). Dissolution kinetics of plagioclase in the melt of the system diopside-albite-anorthite, and origin of dusty plagioclase in andesites. *Contributions to Mineralogy and Petrology*, 89(1), 1-16. doi: 10.1007/BF01177585

Vance, J. A. (1965). Zoning in igneous plagioclase: patchy zoning. *The Journal of Geology*, 73(4), 636-651.

Walker, B. A., Grunder, A. L., & Wooden, J. L. (2010). Organization and thermal maturation of long-lived arc systems: Evidence from zircons at the Aucanquilcha volcanic cluster, northern Chile. *Geology*, *38*(11), 1007-1010. doi: 10.1130/G31226.1

Wanke, M., Clynne, M. A., von Quadt, A., Vennemann, T. W., & Bachmann, O. (2019a). Geochemical and petrological diversity of mafic magmas from Mount St. Helens. *Contributions to Mineralogy and Petrology*, 174, 1-25. doi: 10.1007/s00410-018-1544-4. doi: 10.1007/s00410-018-1542-6

Wanke, M., Karakas, O., & Bachmann, O. (2019b). The genesis of arc dacites: the case of Mount St. Helens, WA. *Contributions to Mineralogy and Petrology*, 174, 1-14.

Wark, D. A., & Watson, E. B. (1993). Plagioclase dissolution and origin of 'patchy' feldspar in igneous rocks. In *Geol Soc Am Abstr Progr* (Vol. 25, pp. 259-260).

Waters, L. E., Andrews, B. J., & Lange, R. A. (2015). Rapid crystallization of plagioclase phenocrysts in silicic melts during fluid-saturated ascent: phase equilibrium and decompression experiments. *Journal of Petrology*, 56(5), 981-1006. doi: 10.1093/petrology/egv025

Waters, L. E., & Lange, R. A. (2015). An updated calibration of the plagioclase-liquid hygrometer-thermometer applicable to basalts through rhyolites. *American Mineralogist*, *100*(10), 2172-2184. doi: 10.2138/am-2015-5232

Wolff, J. A., Ellis, B. S., Ramos, F. C., Starkel, W. A., Boroughs, S., Olin, P. H., & Bachmann, O. (2015). Remelting of cumulates as a process for producing chemical zoning in silicic tuffs: A comparison of cool, wet and hot, dry rhyolitic magma systems. *Lithos*, 236, 275-286.

Zhang, L., & Lüttge, A. (2009). Theoretical approach to evaluating plagioclase dissolution mechanisms. *Geochimica et Cosmochimica Acta*, 73(10), 2832-2849. doi: 10.1016/j.gca.2009.02.021

Table 1: Textural and compositional data for plagioclase crystallised and resorbed in temperature cycling experiments.

Experiment	**22-CSB-03**	**23-CSB-04**	**23-CSB-03**	**23-CSB-07**	**23-CSB-05**
Type	static	single-step heating	single-step heating	single-step heating	Temperature cycling
Temperature increase	-	20°C	30°C	40°C	30°C
Initial growth conditions	168h at 870°C	168h at 870°C	168h at 870°C	168h at 870°C	168h at 870°C
elevated T conditions	-	168h at 890°C	168h at 900°C	168h at 910°C	168h at 900°C
Return to initial conditions	-	-	-	-	168h at 870°C
n_{plag} #	125	359	465	508	219
$A_{plag, tot}$ (mm^2)	0.050	0.066	0.076	0.029	0.073
$l_{Plag, av}$ (µm)	38	25	21	13	31
$A_{plag, av}$ ($µm^2$)	396	185	164	57	335
$V_{plag, av}$ ($µm^3$)	7881	2508	2107	434	6136
S/I $	0.24 ± 0.03	0.29 ± 0.04	0.28 ± 0.04	0.36 ± 0.05	0.28 ± 0.04
R_c^2 $$	0.982	0.988	0.986	0.984	0.992
Surface roughness *	1	1.37	1.64	2.15	1.11
$An_{core, average ± 2SD}$	35.5 ± 2.2	38.4 ± 2.5	38.8 ± 3.1	37.1 ± 4.0	36.8 ± 4.6
$An_{rim/band, max}$ **	-	43.1	47.9	49.2	48.0
$An_{mantle, range}$	-	-	-	-	36 - 40
CaO/Na_2O core, average ± 2SD	1.0 ± 0.1	1.2 ± 0.1	1.2 ± 0.2	1.1 ± 0.2	1.1 ± 0.2
CaO/Na_2O rim/band, max	-	1.4	1.6	1.8	1.7
CaO/Na_2O far-field glass, average ± 2SD	0.3 ± 0.1	0.3 ± 0.1	0.4 ± 0.2	0.5 ± 0.3	0.3 ± 0.1
CaO/Na_2O boundary layer melt, range	-	0.3 - 0.6	0.3 - 1.1	0.4 - 1.2	0.3 - 0.9
CaO/Na_2O melt inclusion, range	-				0.3 - 1.2

# number of plagioclase crystals measured
$ best estimate for 3D short over intermediate axis ± 1SD (Mangler et al., 2022)
$$ R_c^2 - goodness of fit indicator (Mangler et al., 2022)
* average (2D crystal perimeter/area) normalised to value for unresorbed crystals (22-CSB-03)
** average mantle value ± 2SD for cycling experiment 23-CSB-05

1228 **Table 2: 3D shapes of plagioclase crystals in Mount St Helens rocks.**

Sample	Rock type	Crystal zone	Plag resorption type	n_{plag} #	l_{av} (μm)	S $	I $	L $	S/I $	1SD $	R_c^2 $
entire crystal shapes											
MSH90-9	1982 dome dacite	entire	unresorbed	89	129	1.0	3.0	5.2	0.33	0.05	0.976
		entire	surficial	214	303	1.0	2.2	3.6	0.45	0.07	0.991
		entire	pervasive	251	270	1.0	1.4	3.6	0.71	0.08	0.993
MSH-22-56	Castle Creek basalt	entire	unresorbed	321	71	1.0	3.5	5.2	0.29	0.05	0.986
MSH-22-47	Mush enclave	entire	surficial	283	396	1.0	1.6	6.8	0.63	0.06	0.987
MSH-22-57	Mush enclave	entire	surficial	356	126	1.0	2.0	5.6	0.51	0.07	0.979
MSH-22-49	Mush enclave	entire	pervasive	225	249	1.0	1.8	4.8	0.56	0.06	0.991
MSH-22-16	QMI	entire	unresorbed	417	96	1.0	2.7	5.6	0.37	0.06	0.980
MSH-22-20	QMI	entire	unresorbed	411	121	1.0	3.6	5.6	0.28	0.04	0.983
		entire	surficial	167	168	1.0	2.3	4.8	0.43	0.07	0.996
MSH-22-4	QMI	entire	unresorbed	210	124	1.0	3.7	6.4	0.27	0.04	0.994
		entire	surficial	122	156	1.0	3.0	5.0	0.33	0.05	0.997
crystal core and mantle shapes											
MSH90-9	1982 dome dacite	core	surficial	214		1.0	2.3	4.8	0.43	0.07	0.984
		core	pervasive	251		1.0	1.4	3.2	0.71	0.08	0.998
		mantle	surficial	214		1.0	1.8	3.8	0.57	0.07	0.983
		mantle	pervasive	251		1.0	1.5	5.0	0.67	0.07	0.978

MSH – Mount St. Helens; QMI – Quenched Magmatic Inclusion.
# number of plagioclase crystals measured
$ best estimate for 3D crystal shape (Mangler et al., 2022):
S – short axis; I – intermediate axis; L – long axis; 1SD given is for S/I ratio; R_c^2 - goodness of fit indicator.

1229
1230
1231
1232
1233
1234
1235

Figure Captions

Fig. 1: (a) and (b) Back-scattered electron images of typical plagioclase resorption textures using the example of Mount St. Helens. (a) Surficial resorption produced multiple dissolution surfaces with rounded edges in the interior of the crystal. Most oscillatory zones are associated with minor resorption around the edges; arrows designate examples of more significant surficial resorption events. (b) Pervasive resorption of the crystal core produced a sieved texture in the outer core. The morphology of the remaining intact core (dashed outline) does not reflect its original shape and is dominated by deep embayments (arrows). Scale bars are 250 µm in length. (c) and (d) Illustrations of 3D crystal shape terminology used in this study. (c) tabular shape. (d) equant shape.

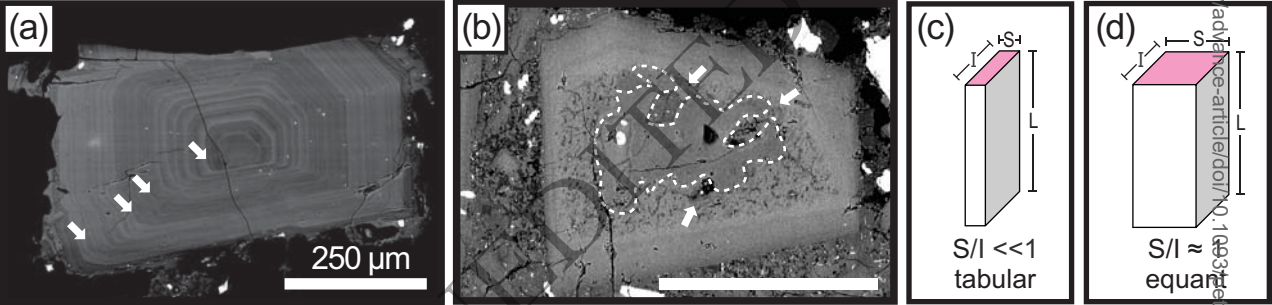
(a)
250 µm
(b)
(c)
S
I
L
S/I <<1
tabular
(d)
S
I
L
S/I ≈
equan

Fig. 2: Graphical illustration of experimental run design. All experiments were conducted under water-saturated conditions and at 150 MPa.

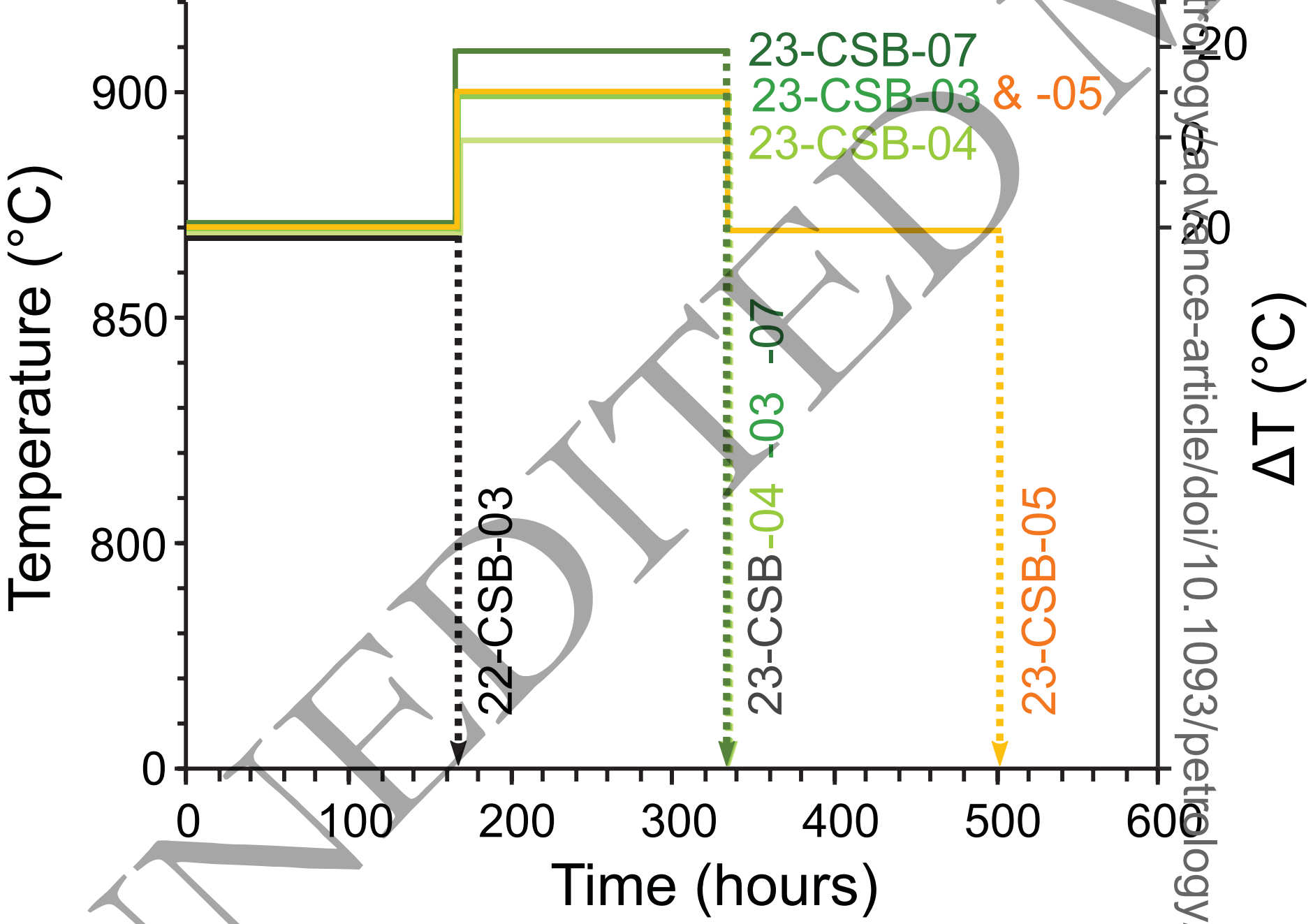

Fig. 3: Representative back-scattered electron images of textures produced in the experimental heating runs. (a) 22-CSB-03. (b) 23-CSB-04. (c) 23-CSB-03. (d) 23-CSB-07. Key features described in the text are annotated. Scale bars are 20 μm in length.

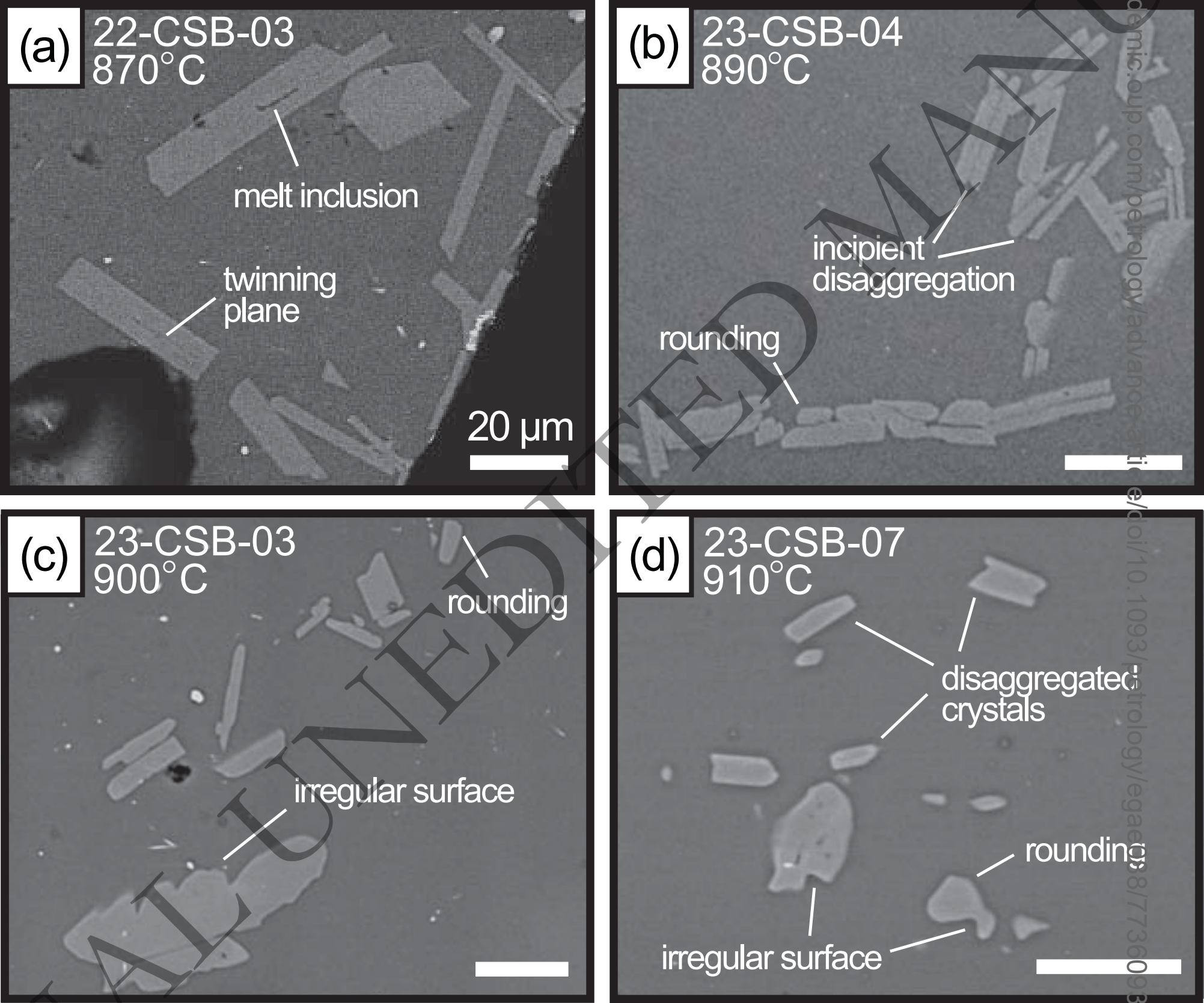

Fig. 4: Normalised frequency plots of 2D crystal aspect ratios (intersection lengths/widths) for the static baseline experiment and the three heating experiments. Heating results in a gradual peak shift from *w/l* ~0.2 to ~0.4, reflecting an increasing number of crystals with lower 2D aspect ratios. The number of plagioclase crystals measured in each experiment are $n = 125$ (CSB-22-03), $n = 359$ (23-CSB-04), $n = 465$ (23-CSB-03), and $n = 508$ (23-CSB-07).

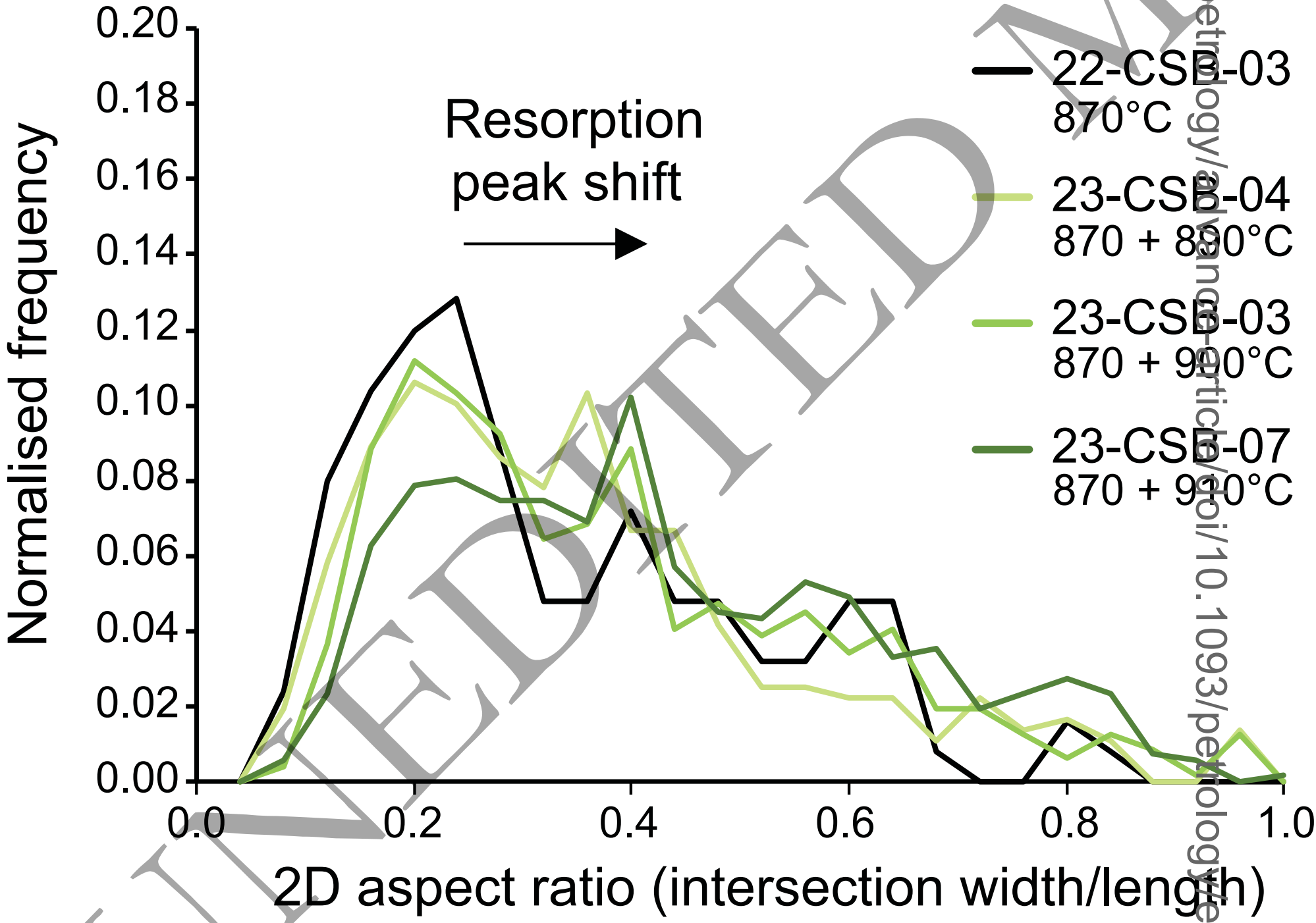

Fig. 5: Textural data for the experimental heating runs plotted as a function of temperature increase. White diamonds: Experiment 22-CSB-03 (870°C, n_{plag} = 125); light green diamonds: 23-CSB-04 (890°C, n_{plag} = 359); mid green diamonds: 23-CSB-03 (900°C, n_{plag} = 465); dark green diamonds: 23-CSB-07 (910°C, n_{plag} = 508). (a) Crystal length ± 95% confidence interval. Symbols larger than error bars except for 22-CSB-03. (b) 3D short/intermediate axis ratio ± 1SD. (c) Surface roughness normalised to mean unresorbed value ± 95% confidence interval. Symbols larger than error bars. (d) mol% An of plagioclase cores and maximum An of plagioclase rims.

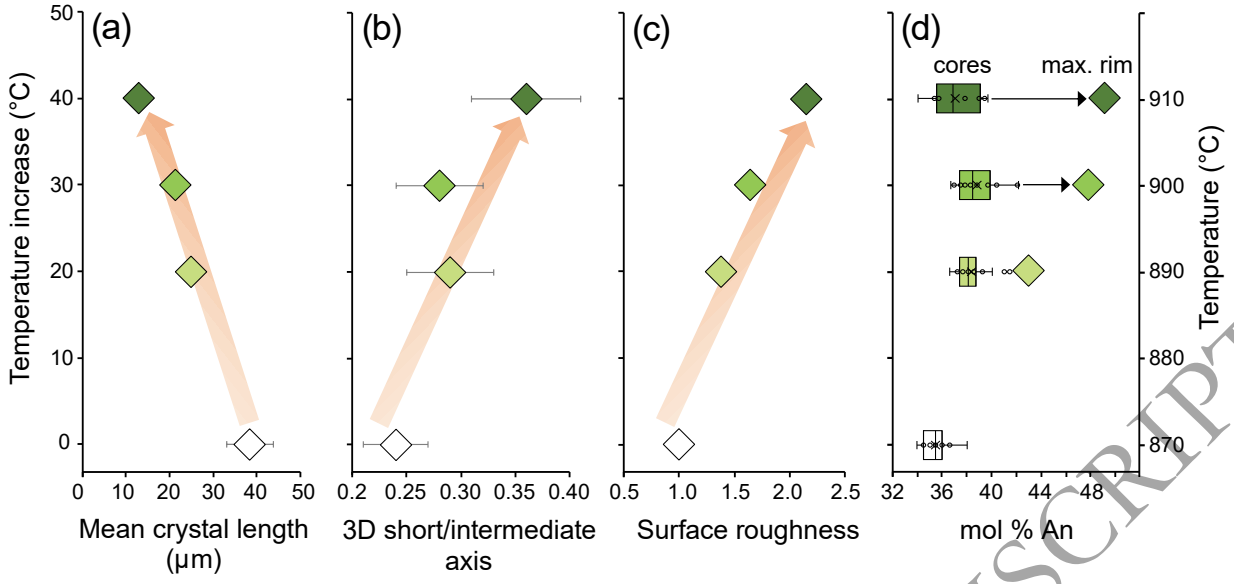

Fig. 6: Enhanced contrast back-scattered electron images of textures produced during heating experiments. Arrows denote surficial resorption (R_s), pervasive resorption (R_p), and growth (G). MI = melt inclusion. Scale bars are 20 μm in length.

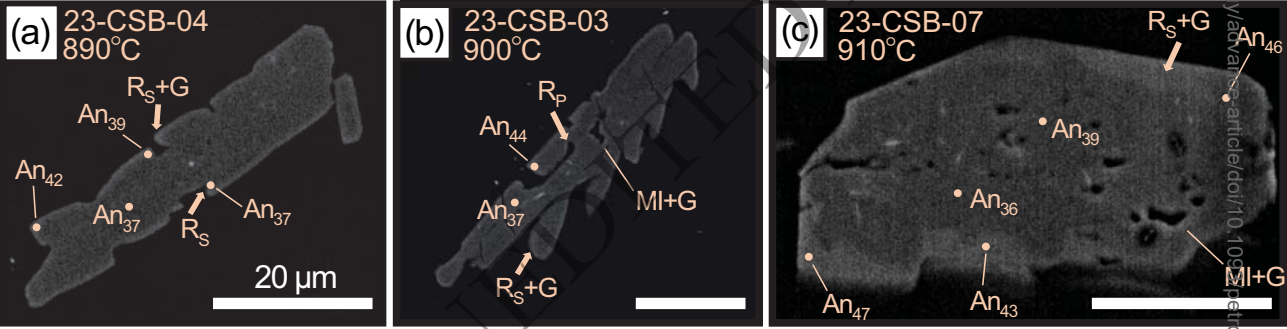
(a)
23-CSB-04
890°C
R_S+G
An_{39}
An_{42}
An_{37}
R_S
An_{37}
20 µm
(b)
23-CSB-03
900°C
R_P
An_{44}
MI+G
An_{37}
R_S+G
(c)
23-CSB-07
910°C
R_S+G
An_{46}
An_{39}
An_{36}
MI+G
An_{47}
An_{43}

Fig. 7: Compositional transects showing Al_2O_3, CaO, and CaO/Na_2O profiles across the crystal-liquid interface in resorbed crystals. At 900°C, plagioclase (Pl) crystals are surrounded by a boundary layer melt (BLM) enriched in dissolved plagioclase components. Boundary layers are typically 2 µm and up to 3.5 µm wide; at greater distances from crystals, melt compositions are unaffected by dissolving plagioclase (far-field melt, FFM). Some plagioclase rims also show 1-2 µm wide rims of elevated CaO and CaO/Na_2O (↑An rim). Error bars in (b) indicate typical analytical uncertainties.

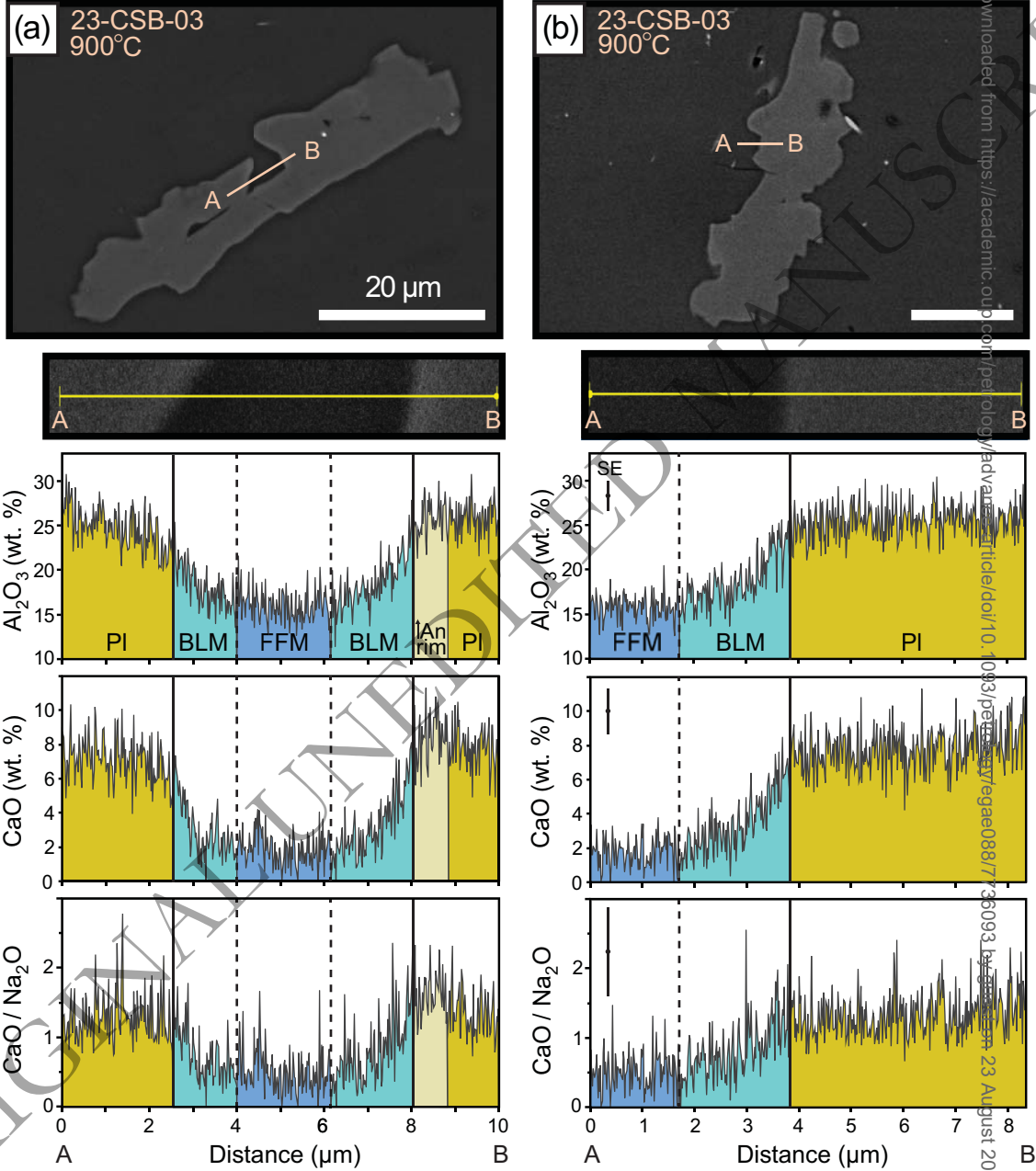

Fig. 8: Crystal textural evolution during a 30°C temperature cycle. Crystals grown at 870°C (white diamonds, 22-CSB-03, n_{plag} = 125) are heated to 900°C and held for one week (green diamonds, 23-CSB-03, n_{plag} = 465) before cooled back down and held at 870°C for another week (yellow diamonds, 23-CB-05, n_{plag} = 219). (a) Crystal length ± 95% confidence interval. (b) 3D short/intermediate axis ratio ± 1SD. (c) Surface roughness ± 95% confidence interval. Note that the while crystal length and surface roughness approach the characteristics of starting plagioclase crystals, 3D crystal aspect ratios do not revert back to original values.

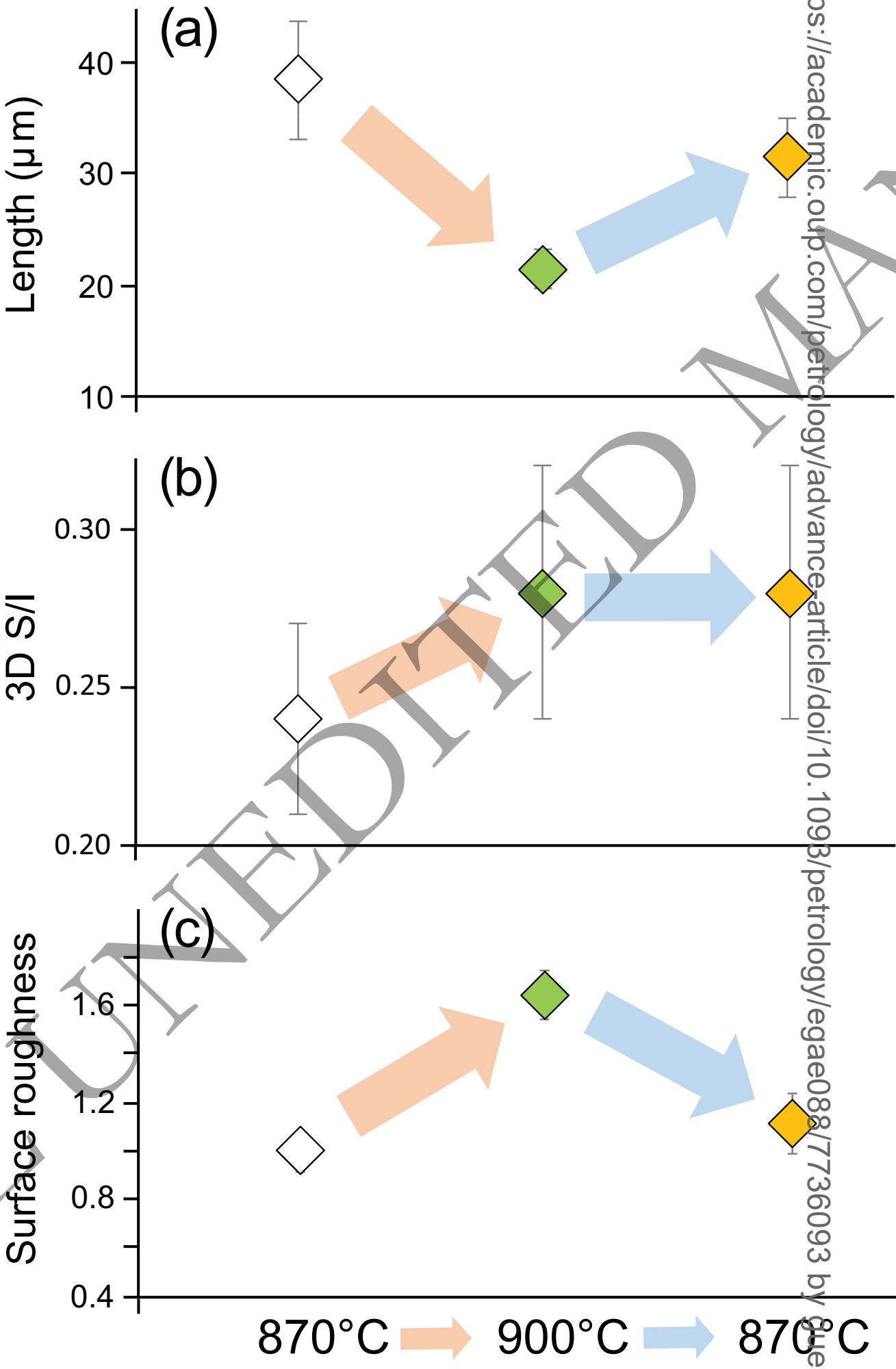

Fig. 9: Enhanced contrast back-scattered electron images of textures produced during the temperature cycling experiment 23-CSB-05. Arrows denote surficial resorption (R_s), pervasive resorption (R_p), growth (G), melt diffusion (D) and intergrowth (IG). C = crystal core; MI = melt inclusion. Orange colours reflect texturally relevant processes at 900°C, blue colours denote processes during cooling to 870°C. Scale bars are 20 µm in length.

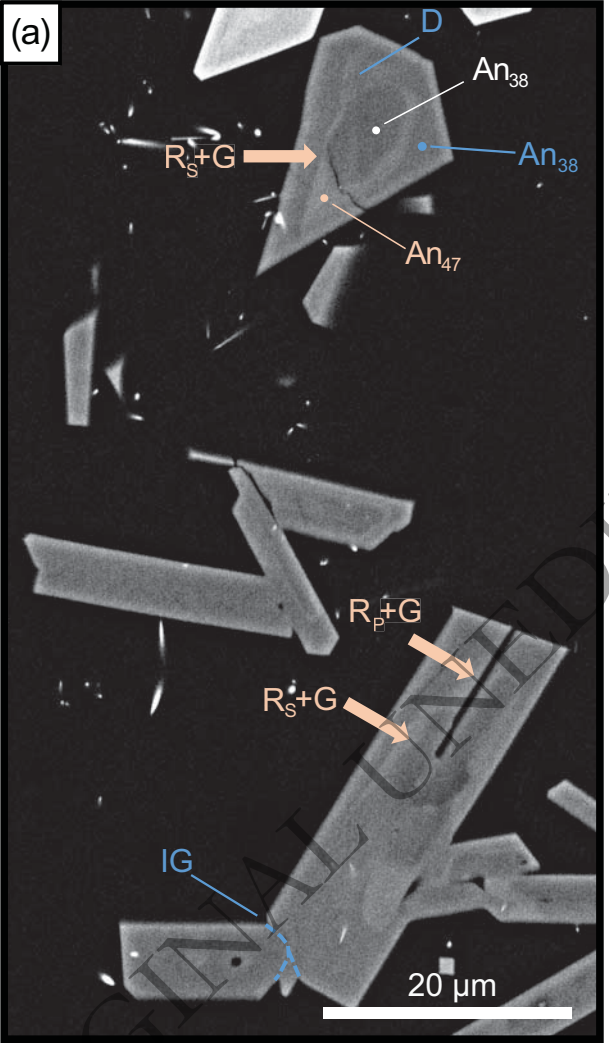

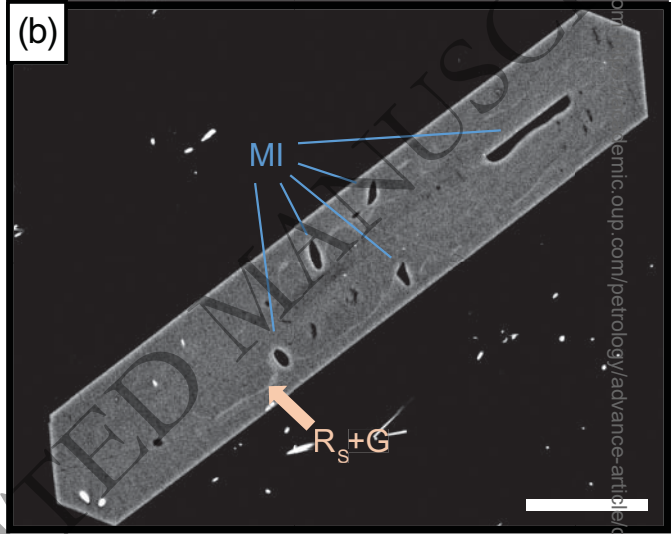

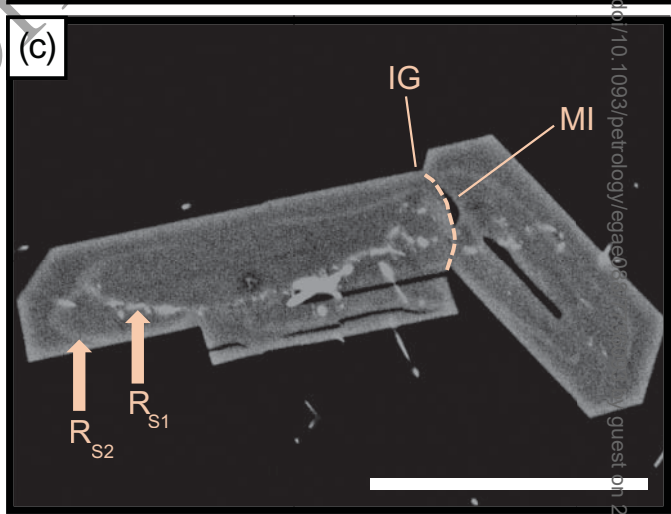

Fig. 10: Enhanced contrast back-scattered electron images of textures produced during the temperature cycling experiment 23-CSB-05. Arrows denote surficial resorption (R_s), pervasive resorption (R_p), growth (G), melt diffusion (D) and intergrowth (IG). C = crystal core; MI = melt inclusion. Orange colours reflect texturally relevant processes at 900°C, blue colours denote processes during cooling to 870°C. Scale bars are 20 µm in length.

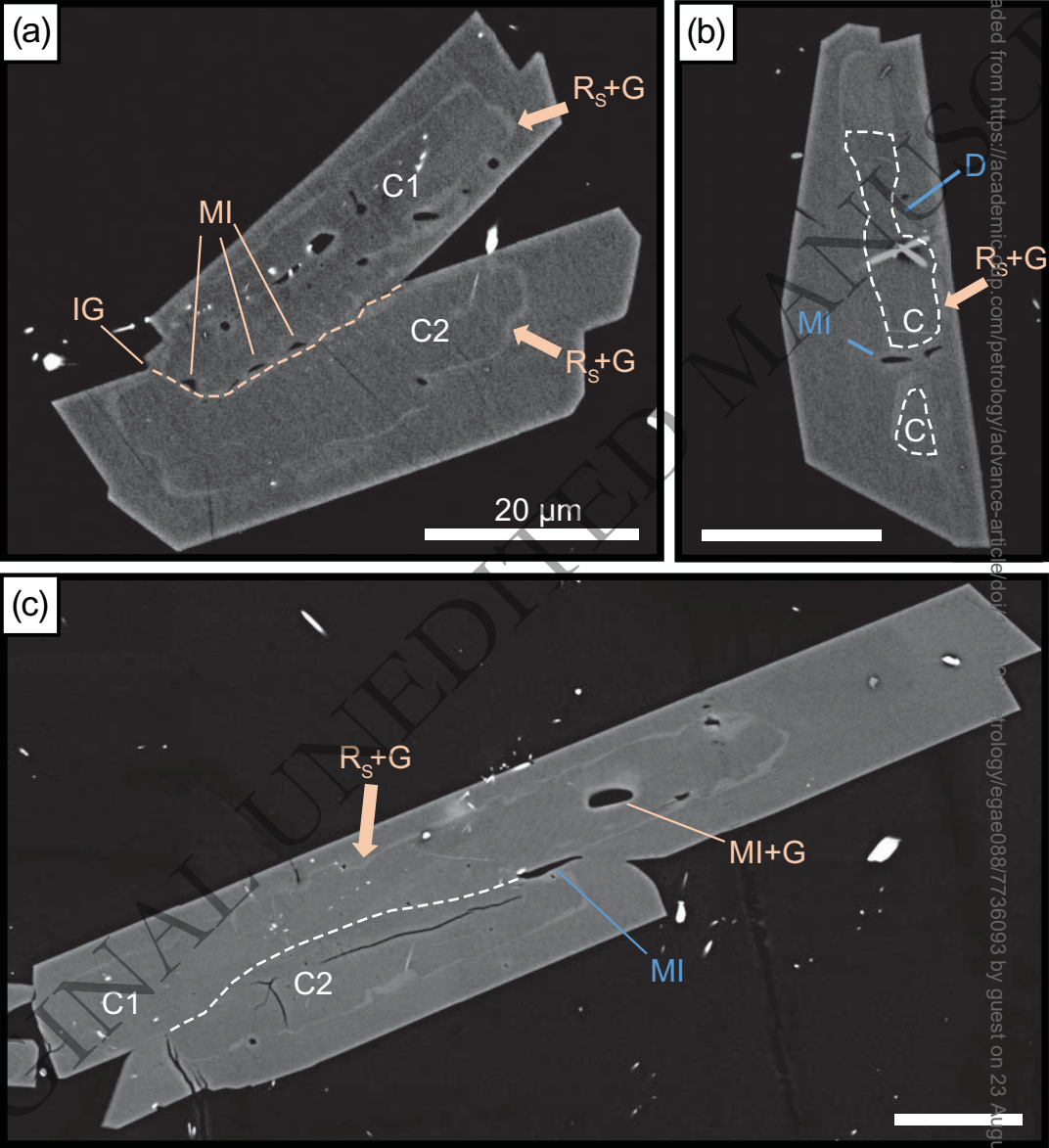

Fig. 11: Schematic showing crystal resorption and growth processes during temperature cycling and their effects on plagioclase textures and compositions. Note that compositional profiles represent idealised transects for illustrative purposes only; back-scattered electron images show respective examples of experimental plagioclase textures and include compositions measured by energy-dispersive X-ray spectroscopy. (a) Initial growth at 870°C produces euhedral crystals (Pl_0) in equilibrium with host melt (M_0). (b) Heating to 900°C results in partial dissolution of Pl_0, formation of a boundary layer melt enriched in Ca/Na (M_1), from which a higher An Pl (Pl_1) recrystallises on rough parts of the dissolution surface. (c) Subsequent cooling to 870°C leads to rapid overgrowth of the resorbed crystal with a mantle which partly records the diffusing boundary layer melt M_1 (Pl_{1b}) before stabilising plagioclase composition characteristic for 870°C ($Pl_2 = Pl_0$). Rapid growth leads to entrapment of abundant melt inclusions which sample the heterogeneous boundary layer melt M_1. See text for discussion.

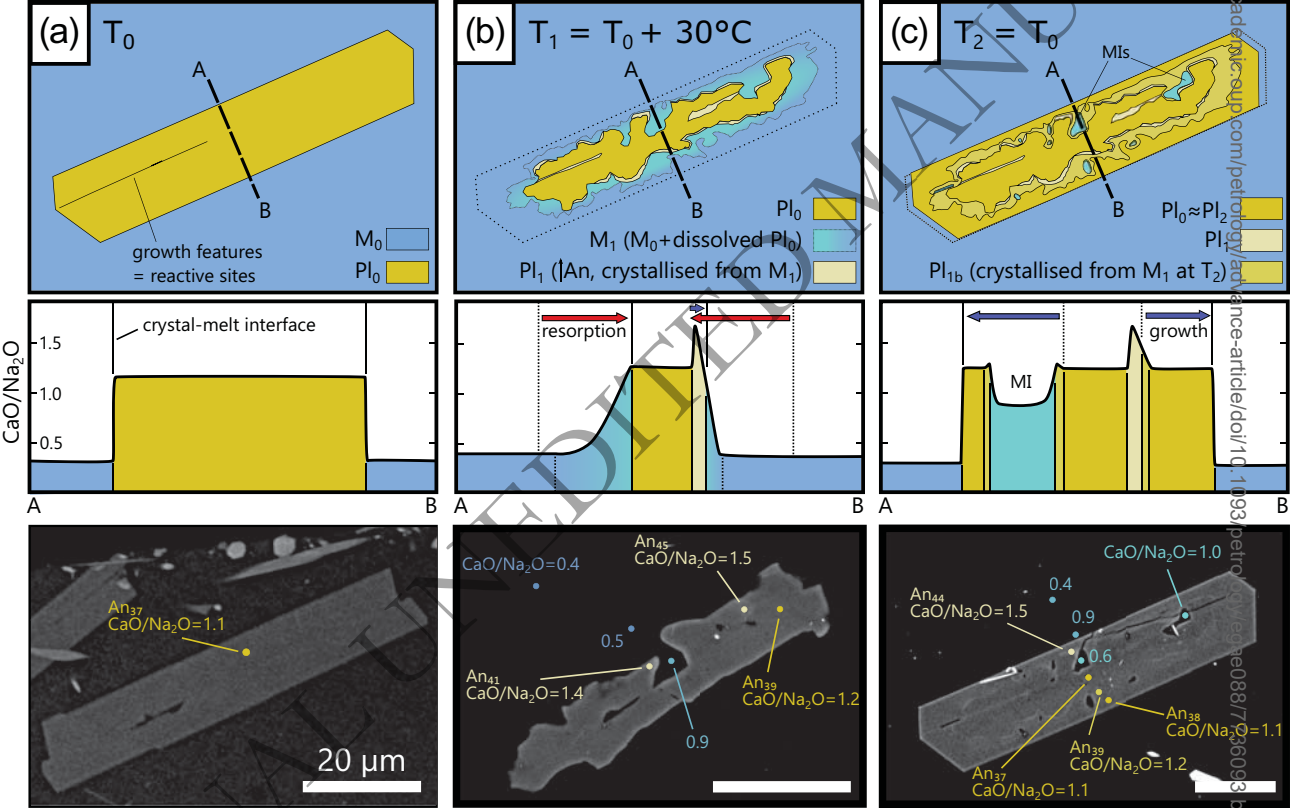

Fig. 12: Mount St. Helens plagioclase Ba and Sr compositions of unresorbed cores, surficially resorbed cores, and pervasively resorbed cores in (a) 1982 dacite, (b) Castle Creek age basalt, (c) quenched melt inclusions (QMI), and (d) mush inclusions. Error bars are 1 SE standard errors of the analyses. Plagioclase compositions overlap with published data for MSH since 1980 (yellow field, Kent et al., 2008) and show no systematic differences between different core types. Published compositional data for tertiary gabbros (green field, Kent et al., 2008) and Cave basalts (orange field, Berlo et al., 2008) are also given.

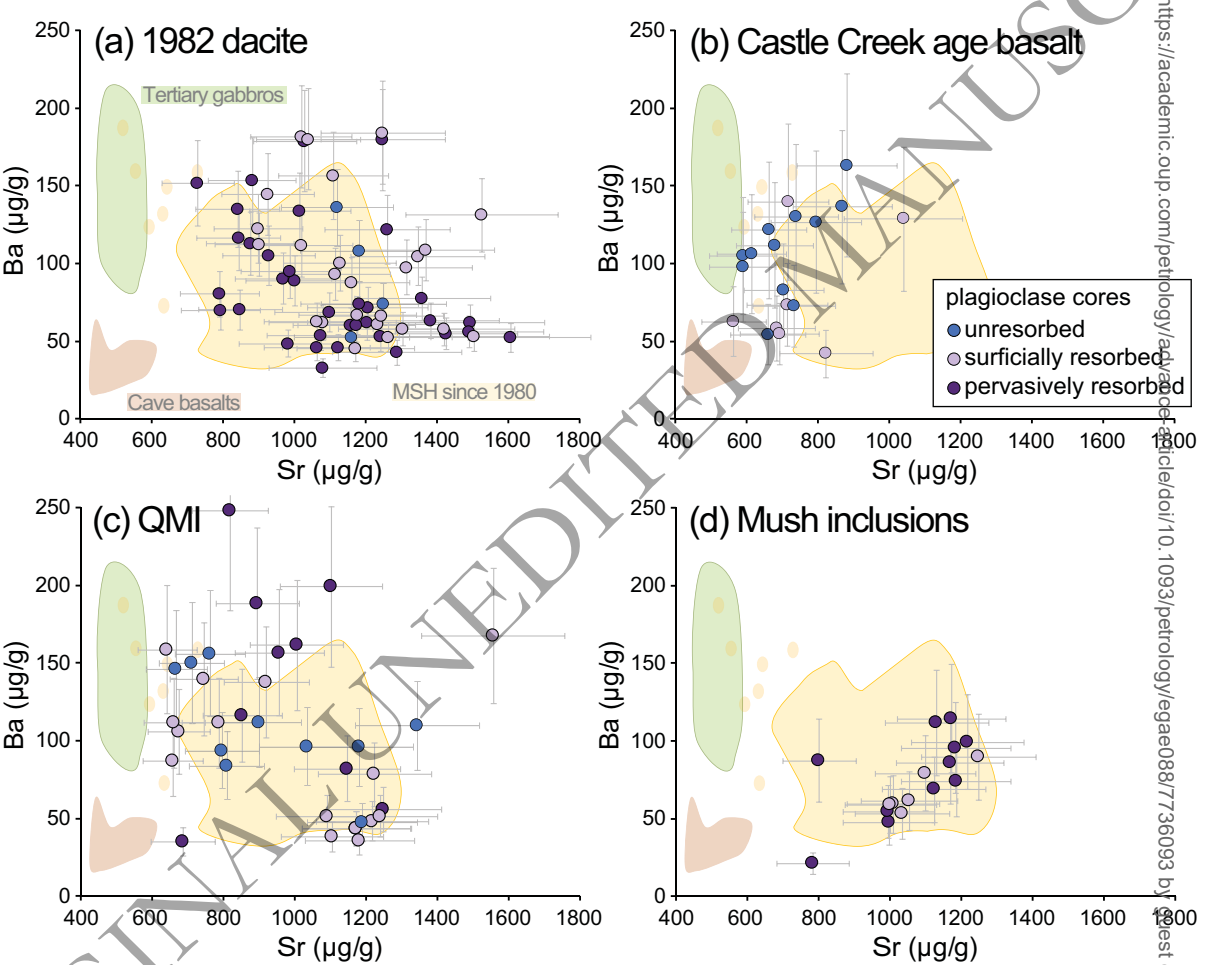

Fig. 13: Representative textures of Mount St. Helens samples. (a) Castle Creek age basalt. (b) Quenched magmatic inclusion (QMI). (c) Mush enclave. (d) 1982 dome dacite. Examples of the three plagioclase categories defined for shape analysis are outlined and labelled; U = unzoned; R_s = surficial resorption; R_p = pervasive resorption. Note the different scale for panel (a).

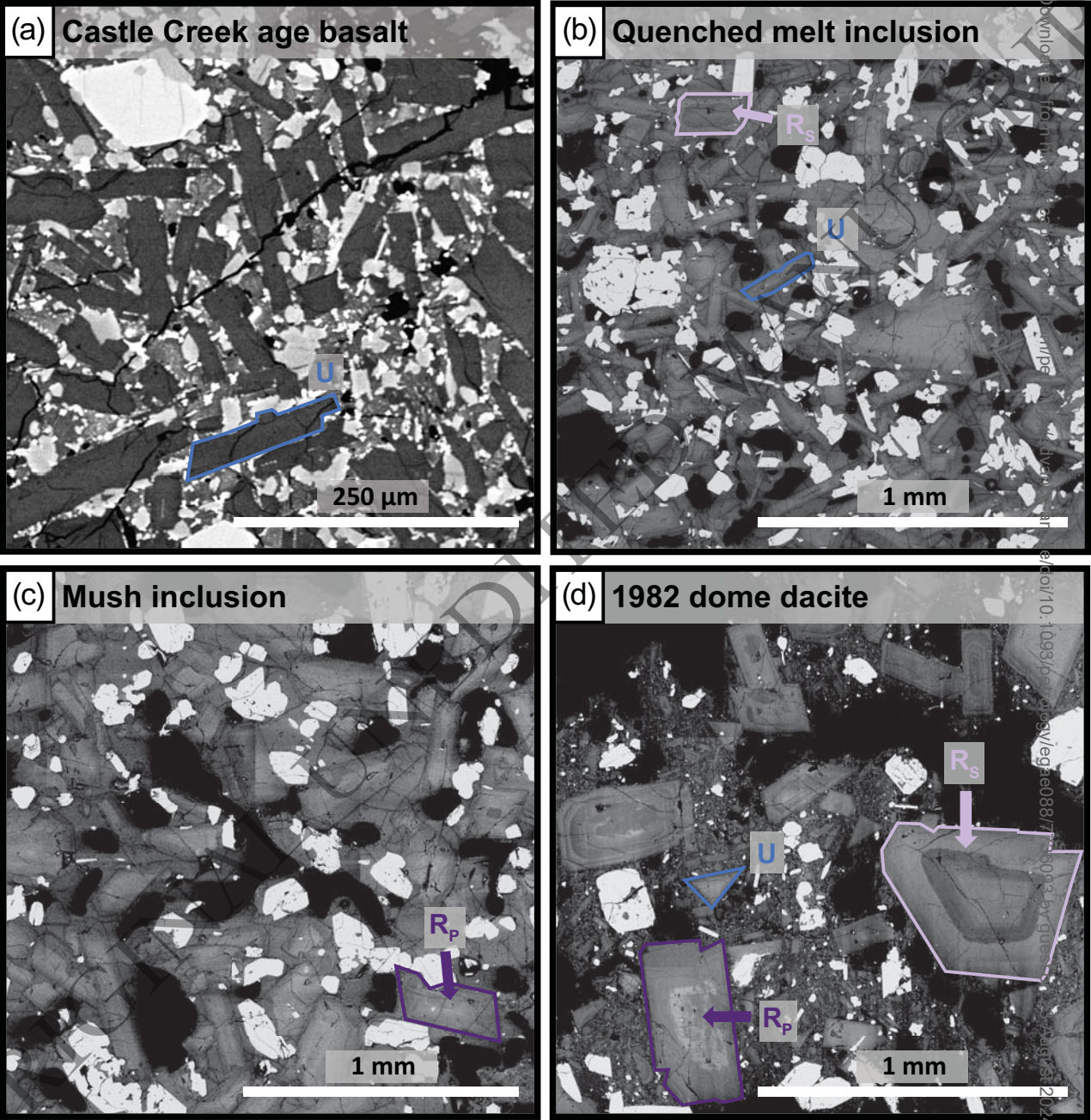
(a)
Castle Creek age basalt
U
250 µm
(b)
Quenched melt inclusion
R_S
U
1 mm
(c)
Mush inclusion
R_P
1 mm
(d)
1982 dome dacite
R_S
U
R_P
1 mm

Fig. 14: Examples of Mount St. Helens plagioclase crystals with textural features akin to resorption experiments. (a) Multiple dissolution surfaces (arrows) associated with rounded edges and roughened surfaces, some of which are associated with melt inclusions (MI). Note the small resorbed crystal which attached to the large plagioclase crystal after one of the last recorded resorption events ("IG"). (b) Two intergrown plagioclase crystals with various dissolution surfaces and a shared outer rim. The triangular shaped crystal next to the intergrown crystals bears striking resemblance to the experimental texture in Fig. 9a. (c) A crystal with two distinct resorbed cores with roughened surfaces (C1 and C2), similar to the experimental texture in Fig. 10c.

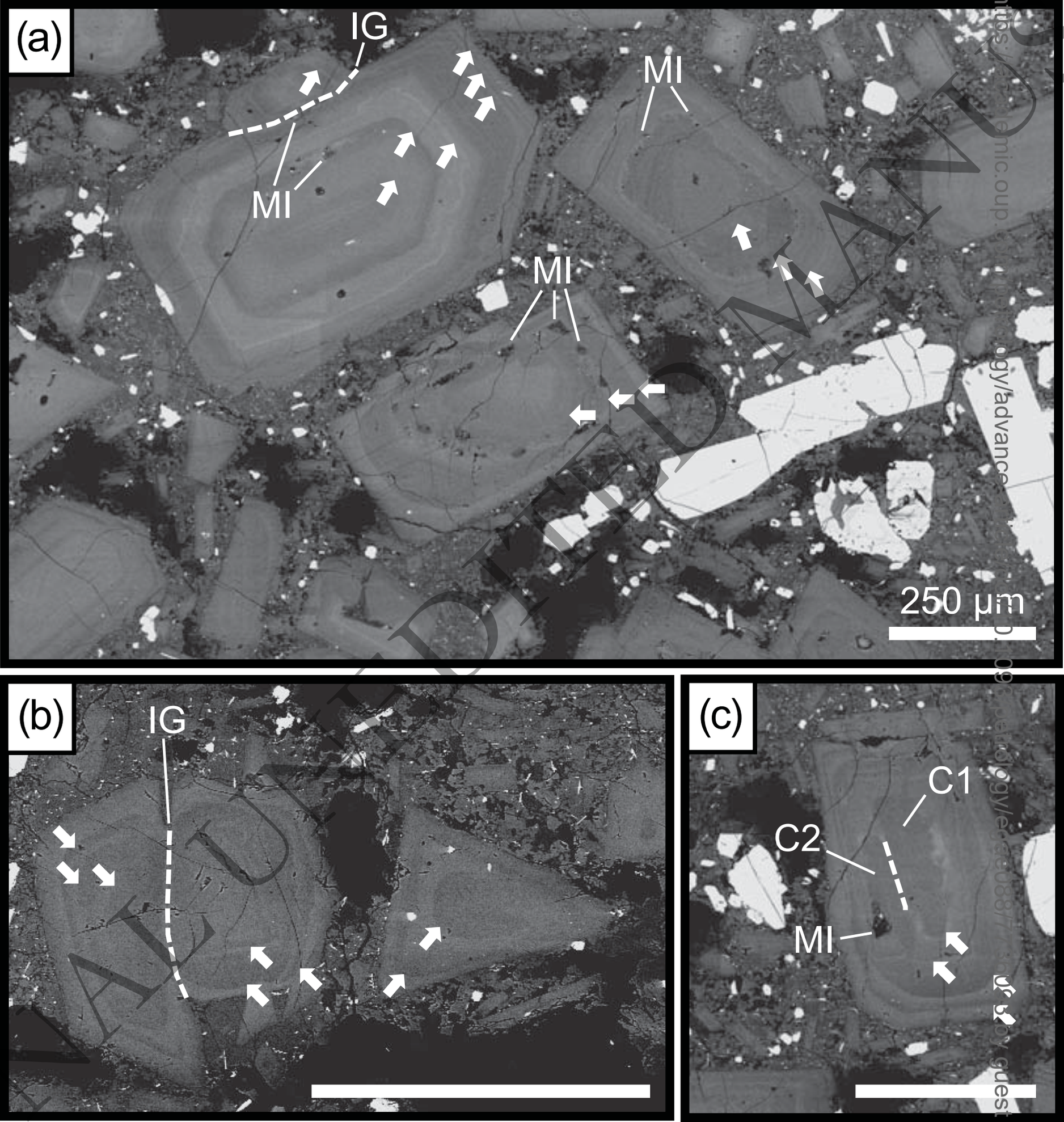

Fig. 15: 3D short/intermediate crystal dimension aspect ratios (*S/I*) ± 1SD of plagioclase crystals in Mount St. Helens samples, distinguished by degree of resorption. (a) Entire MSH sample set. Unresorbed plagioclase crystals show lower *S/I* (i.e., higher aspect ratios) than resorbed crystals. (b) Shapes of crystal cores, mantles and entire crystals of MSH plagioclase crystals in the 1982 dome dacite sample. Entire crystal shapes match those of crystal cores despite distinct mantle growth shapes. See text for discussion.

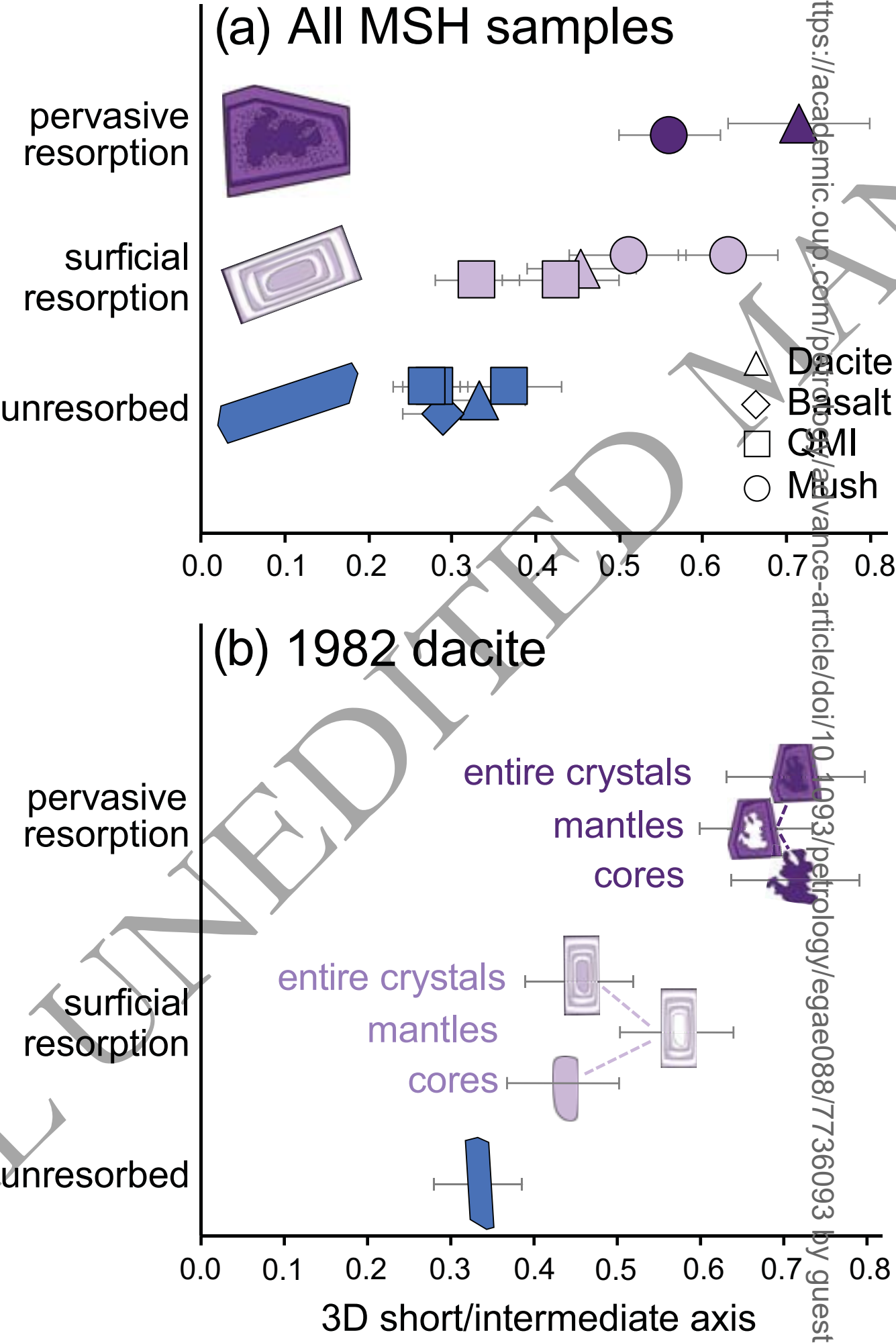

Fig. 16: Schematic model showing the evolution of crystal shapes, lock-up crystallinities, and lock-up temperatures during magma emplacement, mush formation and maturation. T_{liq} = Liquidus temperature; T_{sol} = Solidus temperature; T_{lockup} = Lock-up temperature, i.e. the temperature at which crystallinities reach maximum packing fractions for a given crystal shape and a rheologically locked crystal framework (i.e., mush; blue area) forms. Schematic 3D short/intermediate crystal dimension aspect ratios (*S/I*) for different mush reprocessing stages are shown. Note that with increasing mush maturity, the lockup temperature decreases and the time spent at eruptible magma conditions increases (orange area). Modified after Cooper and Kent (2014).

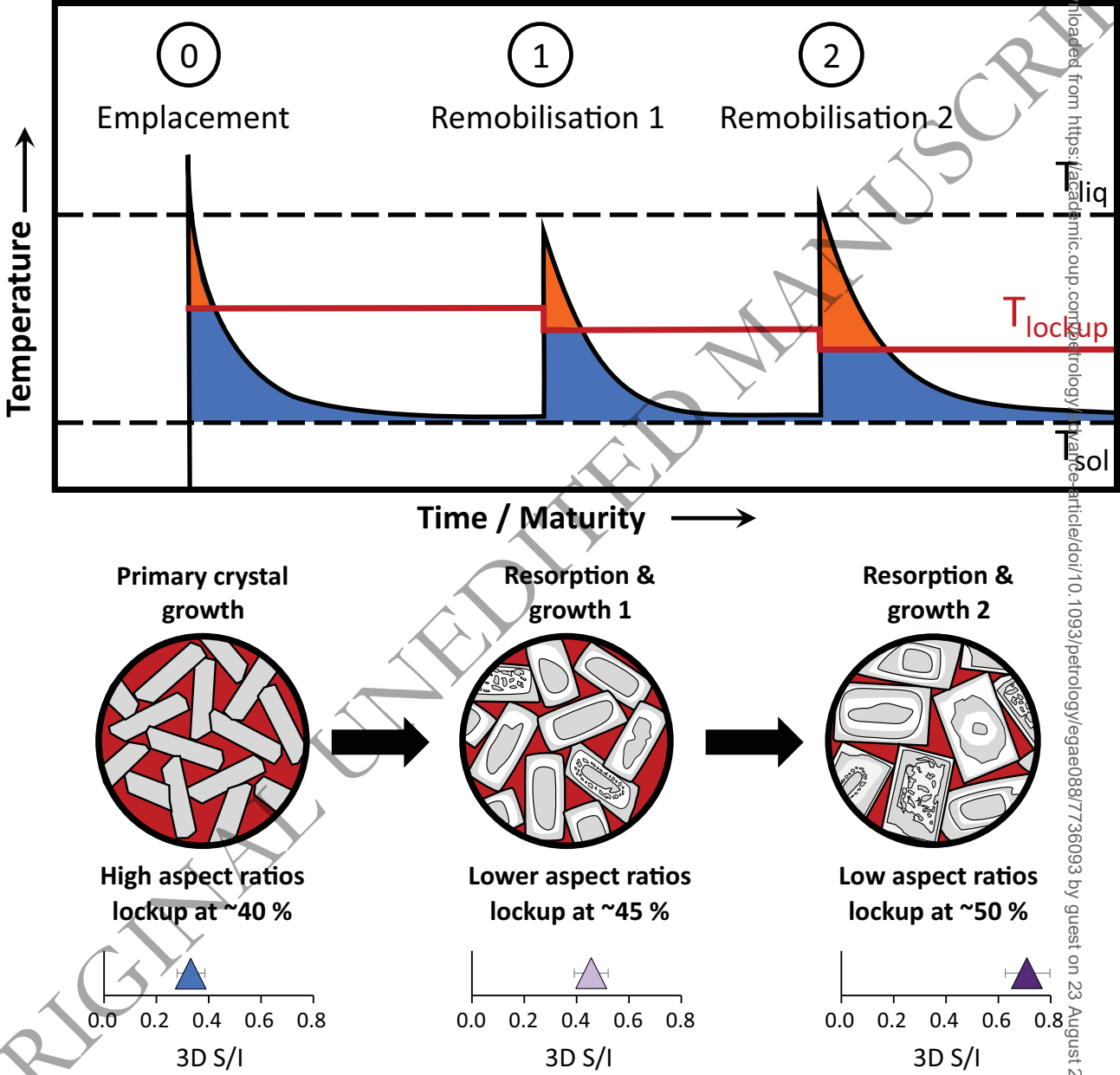

Deltech Furnaces

Sustained operating temperatures to 1800° Celsius

www.deltechfurnaces.com

Gas Mixing System

An ISO 9001:2015 certified company

Custom Vertical Tube

ASME NQA-1 2008 Nuclear Quality Assurance

Standard Vertical Tube

Control systems are certified by Intertek UL508A compliant

Bottom Loading Vertical Tube